Isogeometric Bézier dual mortaring: Refineable higher-order spline dual bases and weakly continuous geometry

Z. Zou[1], M. A. Scott[1], M. J. Borden[1], D. C. Thomas[2], W. Dornisch[3], and E. Brivadis[4]

[1]Department of Civil and Environmental Engineering, Brigham Young University, Provo, Utah 84602, USA
[2]Coreform LLC, P.O. Box 970336, Orem, Utah 84097, USA
[3]Lehrstuhl für Technische Mechanik, Technische Universität Kaiserslautern, Gottlieb-Daimler-Str., Kaiserslautern 67663, Germany
[4]Istituto di Matematica Applicata e Tecnologie Informatiche del CNR, Via Ferrata 1, Pavia 27100, Italy

Abstract

In this paper we develop the isogeometric Bézier dual mortar method. It is based on Bézier extraction and projection and is applicable to any spline space which can be represented in Bézier form (i.e., NURBS, T-splines, LR-splines, etc.). The approach weakly enforces the continuity of the solution at patch interfaces and the error can be adaptively controlled by leveraging the refineability of the underlying slave dual spline basis without introducing any additional degrees of freedom. As a consequence, optimal higher-order convergence rates can be achieved without the need for an expensive shared master/slave segmentation step. We also develop weakly continuous geometry as a particular application of isogeometric Bézier dual mortaring. Weakly continuous geometry is a geometry description where the weak continuity constraints are built into properly modified Bézier extraction operators. As a result, multi-patch models can be processed in a solver directly without having to employ a mortaring solution strategy. We demonstrate the utility of the approach on several challenging benchmark problems.

Keywords: Mortar methods, Isogeometric analysis, Bézier extraction, Bézier projection

1 Introduction

Isogeometric Analysis (IGA), first introduced by Hughes et al. [1], adopts the Computer-aided design (CAD) basis as the basis for analysis. This unifying paradigm has the potential to eliminate the costly geometry clean-up and mesh generation steps which encumber traditional simulation pipelines and improve simulation accuracy through a higher-order smooth basis [1, 2, 3, 4]. To introduce additional flexibility into the isogeometric approach, weak coupling techniques are often used to sew together models composed of multiple patches. These approaches can accommodate patches with differing parameterizations and trimming [5, 6, 7, 8, 9, 10, 11, 12, 13, 14, 15]. However, if not done properly, these coupling techniques can negatively impact the accuracy and robustness of the analysis [5, 6, 15].

In this paper, we present a new local dual mortar method for the coupling of nonconforming higher-order smooth meshes that is based on Bézier extraction and projection [16]. Since it is a biproduct of the Bézier extraction and projection framework, it can be employed during the creation

and editing of geometry through properly modified extraction operators and is applicable to any spline space which has a representation in Bézier form (i.e., NURBS, T-splines, LR-splines, etc.). For this reason, we call the method the isogeometric Bézier dual mortar method. Since the dual basis can be refined in a fashion which is similar to the corresponding spline basis, the error in the method can be adaptively controlled without adding *any* additional degrees of freedom to the linear system. Additionally, optimal higher-order convergence rates can be achieved without the need for an expensive master/slave segmentation step to build a shared mesh over which mortar integrals can be calculated. We feel that this is a critical property for the method to be of practical use in an isogeometric context where complex, smooth, higher-order parameterizations are used for both the master and slave surfaces making segmentation impractical. All numerical examples show that the proposed method works equally well for arbitrary pairings of the master and slave patches. We also develop weakly continuous geometry as an application of dual mortaring in the context of geometric design. A weakly continuous model embeds weak continuity constraints directly into the geometry description. In this way, multi-patch models can be processed in a solver directly, without having to employ a dual mortaring approach during the construction of the linear system.

1.1   A review of weak coupling methodologies

To provide some context and background for the method proposed in this paper, we provide a brief review of existing weak coupling methodologies that have been used in FEA and IGA. There is a vast literature on the subject so only those contributions most closely related to the proposed approach have been included in the overview.

The penalty method [17, 5, 6] weakly imposes a coupling constraint by introducing a penalty term into the variational formulation. It is simple to implement and it does not introduce any additional degrees-of-freedom. The drawback is that, to get an accurate result, a problem and mesh dependent penalty parameter must be selected. This parameter, if not properly adjusted during mesh refinement, results in ill-conditioned linear systems [5].

The Lagrange multiplier method employs a field of Lagrange multipliers to weakly enforce a coupling constraint. For structural mechanics problems, the field of Lagrange multipliers can be interpreted as the traction forces across an interface. In the context of mesh coupling, this method is also called the mortar method [18]. The additional Lagrange multiplier field leads to a saddle point variational formulation, which requires that the Lagrange multiplier space satisfy inf-sup stability and ideally have enough approximability to recover optimal convergence rates [19, 18]. In the context of IGA, the mortar method was first used to couple multiple non-uniform rational B-splines (NURBS) patches by Dornisch et al. [20], and then applied in nonlinear elasticity by Hesch and Betsch [9]. Brivadis et al. [15] explored several choices for the Lagrange multiplier space theoretically and numerically.

The Nitsche method [21], originally introduced for the weak treatment of Dirichlet boundary conditions, is a method that has a variational structure between the Lagrange multiplier and penalty methods. In this approach, the Lagrange multiplier in the variational formulation is replaced by the normal flux, and an extra penalty-like stabilization term is added to restore the coercivity of the bilinear form. This method has been applied to the coupling of non-conforming meshes in many areas, including IGA [12, 5, 7, 8]. Like the penalty method, the stabilization term contains a parameter which must be estimated [5].

The approach proposed in [22, 23] embeds the coupling constraints into the finite element space directly, thus leading to a positive definite nonconforming variational problem. Based on [22, 23], Wohlmuth [24, 25] then proposed a local dual Lagrange multiplier space and called the resulting formulation a dual mortar method. In contrast to a standard Lagrange multiplier method, in a dual

mortar method the Lagrange multipliers can be eliminated easily leading to greater computational efficiency. In addition, the compact support of the local dual basis along with the biorthogonality preserves the sparsity of the stiffness matrix. Unfortunately, it is not easy to construct a local dual basis that possesses a high-order polynomial reproduction property [26, 27].

Dornisch et al. [10] developed a dual mortar method based on a global B-spline dual basis, and derived a relation matrix which enabled a condensation of the Lagrange multiplier degrees-of-freedom. A similar relation matrix is derived by Coox et al. [11] by inserting virtual knots on either side of an interface. This method is mathematically identical to the global dual method in [10] but is more efficient. However, it is limited to the case where the neighboring patches have the same degree and parameterization along the interface, which is a very restrictive requirement. Seitz et al. [13] proposed a local dual mortar method based on a NURBS basis for both patch coupling and contact mechanics. In this case, the local dual basis does not satisfy the polynomial reproduction property, so only reduced convergence rates are obtained. Other types of local dual basis functions, such as, the explicit de Boor-Fix dual basis [28, 29, 30] and the approximate dual basis [31] are explored in [14]. The de Boor-Fix dual basis functions have the same support as the B-spline basis functions. However, the polynomial reproduction property does not hold, leading to significantly deteriorated convergence rates. The approximate dual basis fulfills the polynomial reproduction property but not biorthogonality. Therefore, the fully populated inverse matrix of the original mortar matrix must be approximated by a diagonal matrix to maintain the locality. This implies that the coupling constraints are not imposed exactly. Even though several numerical examples show that the approximate dual mortar method achieves convergence rates which are comparable to the global dual mortar method, a mathematical analysis of the effects of the approximation is still missing.

The outline of this paper is as follows. In Section 2, we briefly review fundamental concepts for splines and dual bases which are needed throughout the paper. Section 3 describes multi-patch domain decomposition and the model problem we will use to define our method. Isogeometric Bézier dual mortaring is then described in Section 4. We then define weakly continuous geometry and its relationship to Bézier dual mortaring in Section 5. Several challenging benchmark problems are solved in Section 6 to illustrate the properties of the method. We then draw conclusions in Section 7.

2 Spline fundamentals and dual bases

2.1 Bézier, B-spline, and NURBS fundamentals

The ith Bernstein polynomial of degree p on $[\xi_1, \xi_2]$ can be defined as

$$B_{i,p}(\xi) = \binom{p}{i-1} \left(\frac{\xi_2 - \xi}{\xi_2 - \xi_1} \right)^{p-i+1} \left(\frac{\xi - \xi_1}{\xi_2 - \xi_1} \right)^{i-1}, \tag{1}$$

where $\binom{p}{i-1} = \frac{p!}{(i-1)!(p-i+1)!}$ is the binomial coefficient.

The set of Bernstein polynomials $\mathbf{B}(\xi) = \{B_{i,p}(\xi)\}_{i=1}^{p+1}$ forms a basis for the space of polynomials of degree p. The Bernstein polynomials $\tilde{\mathbf{B}}(\tilde{\xi})$ defined on $[\tilde{\xi}_1, \tilde{\xi}_2]$, can be related to the Bernstein basis $\mathbf{B}(\xi)$ defined on $[\xi_1, \xi_2]$ through the relation

$$\tilde{\mathbf{B}}(\tilde{\xi}) = (\mathbf{M})^{-\mathrm{T}} \mathbf{B}(\xi) \tag{2}$$

3

with $\mathbf{M}$ the transformation matrix. A formula for the inverse of the transformation matrix $\mathbf{M}$ can be found in [32] and is written as

$$(M)_{jk}^{-1} = \sum_{l=\max(1,j+k-p-1)}^{\min(j,k)} B_{l,j-1}(\xi_2) B_{k-l+1,p-j+1}(\xi_1), \qquad 1 \leq j,k \leq p+1. \tag{3}$$

A degree p Bézier curve in $\mathbb{R}^d$ can be written as

$$\mathbf{x}(\xi) = \sum_{i=1}^{p+1} \mathbf{P}_i \, B_{i,p}(\xi), \qquad \xi \in [\xi_1, \xi_2] \tag{4}$$

where $\mathbf{P}_i$ is called a control point. A univariate B-spline basis is defined by a knot vector $\Xi = \{\xi_1, \xi_2, \ldots, \xi_{n+p+1}\}$, which consists of a non-decreasing sequence of real numbers, $\xi_i \leq \xi_{i+1}, i = 1, \ldots, n+p+1$, where p is the degree of the B-spline basis functions and n is the number of basis functions. The ith B-spline basis function of degree p, denoted by $N_{i,p}(\xi)$, can be recursively defined by

$$N_{i,0}(\xi) = \begin{cases} 1, & \text{if} \quad \xi_i \leq \xi < \xi_{i+1} \\ 0, & \text{otherwise} \end{cases}$$

$$N_{i,p}(\xi) = \frac{\xi - \xi_i}{\xi_{i+p} - \xi_i} N_{i,p-1}(\xi) + \frac{\xi_{i+p+1} - \xi}{\xi_{i+p+1} - \xi_{i+1}} N_{i+1,p-1}(\xi).$$

A B-spline curve can be viewed as the smooth composition of multiple Bézier curves. A B-spline curve of degree p can be written as

$$\mathbf{x}(\xi) = \sum_{i=1}^{n} \mathbf{P}_i N_{i,p}(\xi), \qquad \xi \in [\xi_1, \xi_{n+p+1}] \tag{5}$$

and a pth-degree NURBS curve can be written as

$$\mathbf{x}(\xi) = \sum_{i=1}^{n} \mathbf{P}_i w_i R_{i,p}(\xi), \qquad \xi \in [\xi_1, \xi_{n+p+1}] \tag{6}$$

where the NURBS basis function $R_{i,p}$ is defined by

$$R_{i,p}(\xi) = \frac{N_{i,p}(\xi)}{W(\xi)} \tag{7}$$

where $N_{i,p}(\xi)$ is the ith p-degree B-spline basis functions,

$$W(\xi) = \sum_{i=1}^{n} w_i N_{i,p}(\xi) \tag{8}$$

is the weighting function, and w_i is the weight corresponding to $N_{i,p}(\xi)$. Since a NURBS curve is a rational polynomial it can be used to exactly represent conic sections. Higher dimensional analogs to these concepts can be created using tensor products or more advanced construction schemes like T-splines or hierarchical B-splines.

4

2.2 Bézier extraction

The Bézier extraction process [33, 34] generates a linear operator, called the extraction operator, that maps a Bernstein basis onto a B-spline basis. In the context of one-dimensional B-splines, the extraction operator encodes the result of repeated knot insertion [35] such that the multiplicity of all interior knots of a knot vector is $p+1$. At the element level, the resulting linear transformation, $\mathbf{C}^e$, is called the element extraction operator. This element-level operator is used to map a Bernstein basis $\mathbf{B}$ defined over an element e onto a B-spline basis restricted to that same element. In other words, $\mathbf{N}^e = \mathbf{C}^e \mathbf{B}$. See [33, 34] for additional details.

2.3 Dual bases

Suppose $\mathcal{B}_p$ is a $(p+1)$-dimensional linear space generated by a set of linearly independent functions $\{b_i\}_{i=1}^{p+1}$ of maximal degree p. Given an inner product $(\cdot, \cdot) \colon \mathcal{B}_p \times \mathcal{B}_p \mapsto \mathbb{R}$, the functions from the set

$$\boldsymbol{\lambda}_p := \{\lambda_i\}_{i=1}^{p+1} \tag{9}$$

satisfying the following conditions

$$\begin{cases} \operatorname{span} \boldsymbol{\lambda}_p = \mathcal{B}_p, \\ (b_i, \lambda_j) = \delta_{ij}, \quad 1 \le i, j \le p+1 \end{cases} \tag{10}$$

form the so-called dual basis corresponding to the basis $\{b_i\}_{i=1}^{p+1}$ with respect to the inner product $(\cdot, \cdot)$. The first condition in (10) is called the reproduction property of order p and the second property is called the biorthogonality property. With local dual mortar method, $(p-1)$-order reproduction property of the Lagrange multiplier space is required to guarantee the optimality of the finite element space of order p [27].

3 Problem description

3.1 Domain decomposition

Let Ω be a bounded domain decomposed into K non-overlapping subdomains Ω^k, i.e.,

$$\overline{\Omega} = \bigcup_{k=1}^{K} \overline{\Omega}^k, \text{ and } \Omega^i \cap \Omega^j = \emptyset, i \ne j.$$

We define the interfaces as the interior of the intersections of the boundaries, i.e., $\Gamma^\ell = \partial \Omega^i \cap \partial \Omega^j$. On each Ω^k the solution space $\mathcal{S}^k$ is defined as

$$\mathcal{S}^k = \{\mathbf{u}^k \in H^1(\Omega^k), \mathbf{u}^k|_{\partial \Omega \cap \partial \Omega^k} = \mathbf{u}_0\}$$

where $H^1(\Omega^k)$ are the standard Sobolev spaces and $\mathbf{u}_0$ are the Dirichlet boundary conditions. The corresponding weighting function spaces, $\mathcal{V}^k$, are similarly defined with homogeneous boundary conditions on $\partial \Omega \cap \partial \Omega^k$. The displacement solution space on Ω is then the broken Sobolev space $\mathcal{S}$ defined as $\mathcal{S} = \prod_{k=1}^{K} \mathcal{S}^k$, along with continuity conditions defined along the interfaces. To simplify the exposition of the proposed mortaring technique, we employ a two-patch geometry with one interface, i.e., $K = 2$. The interface is denoted as $\Gamma = \partial \Omega^m \cap \partial \Omega^s$, where the superscripts m and s are used to denote the master and slave patches, respectively.
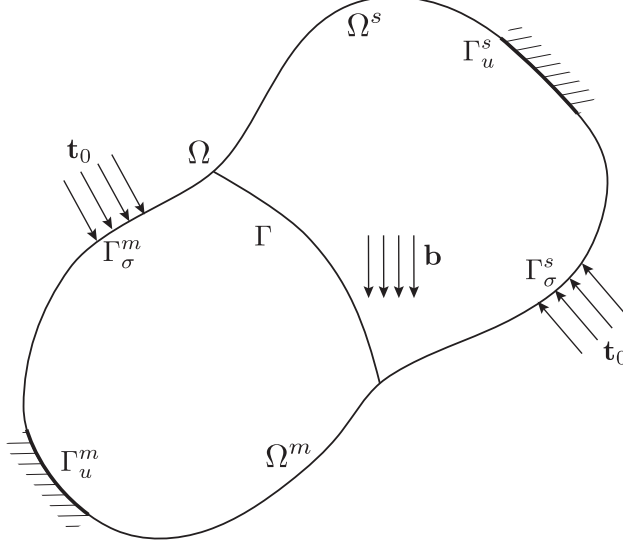
Figure 1: A schematic of the linear elastic model problem.

3.2 A linear elastic model problem

To ground our approach in a practical example, we consider the following linear elasticity problem:

$$\text{div } \boldsymbol{\sigma} + \mathbf{b} = 0 \quad \text{in } \Omega = \Omega^m \cup \Omega^s \tag{11a}$$

$$\mathbf{u} = \mathbf{u}_0 \quad \text{on } \Gamma_u = \Gamma_u^m \cup \Gamma_u^s \tag{11b}$$

$$\boldsymbol{\sigma} \cdot \mathbf{n} = \mathbf{t}_0 \quad \text{on } \Gamma_\sigma = \Gamma_\sigma^m \cup \Gamma_\sigma^s \tag{11c}$$

$$\mathbf{u}^m = \mathbf{u}^s \quad \text{on } \Gamma \tag{11d}$$

where $\Gamma_u \cap \Gamma_\sigma = \emptyset$, $\Gamma_u \cap \Gamma = \emptyset$, $\Gamma_\sigma \cap \Gamma = \emptyset$, $\boldsymbol{\sigma}$ is the stress tensor, $\mathbf{b}$ is the body force, $\mathbf{u}_0$ and $\mathbf{t}_0$ are the prescribed Dirichlet and Neumann boundary conditions applied on Γ_u and Γ_σ, respectively and $\mathbf{n}$ is the unit outward normal vector on $\partial\Omega$, see Figure 1. The kinematic coupling condition $\mathbf{u}^m = \mathbf{u}^s$ is introduced along the interface Γ where $\mathbf{u}^m$ and $\mathbf{u}^s$ are the master and slave interface displacements, respectively.

The total potential energy Π of the system Ω is

$$\Pi(\mathbf{u}) = \Pi^m(\mathbf{u}^m) + \Pi^s(\mathbf{u}^s) + \int_{\hat{\Gamma}} \boldsymbol{\Phi} \cdot (\mathbf{u}^m - \mathbf{u}^s) \, \mathrm{ds} \tag{12}$$

where Π^m and Π^s are the potential energy on Ω^m and Ω^s, respectively, and $\boldsymbol{\Phi}$ is a Lagrange multiplier weakly enforcing the continuity constraint along the interface. Invoking the stationarity of Π with respect to $\mathbf{u}^m$, $\mathbf{u}^s$ and $\boldsymbol{\Phi}$, we obtain the weak formulation of (11) that reads as: find $\mathbf{u}^m \in \mathcal{S}^m$, $\mathbf{u}^s \in \mathcal{S}^s$ and $\boldsymbol{\Phi} \in \mathcal{S}^\ell$ such that for all variations $\delta\mathbf{u}^m \in \mathcal{V}^m$, $\delta\mathbf{u}^s \in \mathcal{V}^s$ and $\delta\boldsymbol{\Phi} \in \mathcal{V}^\ell$

$$\delta\Pi^*(\mathbf{u}, \delta\mathbf{u}^m) = \delta\Pi^m(\mathbf{u}^m, \delta\mathbf{u}^m) + \int_{\hat{\Gamma}} \boldsymbol{\Phi} \cdot \delta\mathbf{u}^m \, \mathrm{d}\Gamma = 0 \tag{13a}$$

$$\delta\Pi^*(\mathbf{u}, \delta\mathbf{u}^s) = \delta\Pi^s(\mathbf{u}^s, \delta\mathbf{u}^s) - \int_{\hat{\Gamma}} \boldsymbol{\Phi} \cdot \delta\mathbf{u}^s \, \mathrm{d}\Gamma = 0 \tag{13b}$$

$$\delta\Pi^*(\mathbf{u}, \delta\boldsymbol{\Phi}) = \int_{\hat{\Gamma}} \delta\boldsymbol{\Phi} \cdot (\mathbf{u}^m - \mathbf{u}^s) \, \mathrm{ds} = 0 \tag{13c}$$

6

where $\mathcal{S}^m$, $\mathcal{S}^s$ and $\mathcal{S}^\ell$ are the displacement solution approximation spaces on Ω^m and Ω^s and the Lagrange multiplier space, respectively, and $\mathcal{V}^m$, $\mathcal{V}^s$ and $\mathcal{V}^\ell$ are the corresponding weighting function spaces. Note that in (12) we define the interface energy on the parametric domain of the slave interface, denoted by $\hat{\Gamma}$, which results in the interface continuity condition (13c). As will be shown subsequently, this will allow us to define a dual basis which is independent of geometry, an important simplification which improves the efficiency of the approach.

4   Isogeometric Bézier dual mortaring

We will choose the Lagrange multiplier spaces to be those spanned by a dual spline basis defined over $\hat{\Gamma}$ which emanate from the Bézier extraction and projection framework. A weighted dual basis for each element domain $\hat{\Gamma}^e$ is defined as

$$\bar{\mathbf{N}}^e = \mathrm{diag}(\boldsymbol{\omega}^e)(\mathbf{R}^e)^T(\mathbf{G}_{B,B}^e)^{-1}\mathbf{B}^{e,s} \tag{14}$$

$$= \mathbf{D}^e\mathbf{B}^{e,s} \tag{15}$$

where $\mathbf{B}^{e,s}$ is the set of Bernstein polynomials defined on the eth slave interface element and

$$\mathbf{G}_{B,B}^e = \left[\int_{\hat{\Gamma}^e} B_i^{e,s}(\xi^s)B_j^{e,s}(\xi^s)\,ds\right] \tag{16}$$

is the Gramian matrix for the Bernstein basis [16?], $\mathbf{R}^e$ is the element reconstruction operator [16] and $\mathbf{D}^e$ is called a dual element extraction operator. Note that $\mathbf{R}^e$ is restricted to the element boundary $\hat{\Gamma}^e$. We use the standard Bézier projection weighting, i.e.,

$$\omega_i^e = \frac{\int_{\hat{\Gamma}^e} N_i^{e,s}\,ds}{\int_{\hat{\Gamma}^I} N_{I(i,e)}^s\,ds} \tag{17}$$

where $\hat{\Gamma}^I$ is the domain of support for the interface basis function N_I^s and $I(i,e)$ is a standard mapping from element nodal indexing to a global index I. While other weightings could be used this weighting has been shown to give particularly accurate results [16]. We can easily show that the proposed dual basis satisfies the biorthogonality condition (10) by noting that

$$\int_{\hat{\Gamma}^e} \bar{\mathbf{N}}^e(\mathbf{N}^{e,s})^T ds = \mathrm{diag}(\boldsymbol{\omega}^e) \tag{18}$$

and

$$\underset{e}{\mathsf{A}}\left[\int_{\hat{\Gamma}^e} \bar{\mathbf{N}}^e(\mathbf{N}^{e,s})^T\,ds\right] = \mathbf{I}. \tag{19}$$

where A is the usual finite element assembly operator. In other words,

$$\int_{\hat{\Gamma}} \bar{N}_I N_J^s ds = \delta_{IJ} \tag{20}$$

as desired.

Note that even though this dual basis does not possess a higher-order polynomial reproduction property [36], optimal higher-order rates can be easily recovered through a simple refinement step. A theoretical explanation for this behavior is beyond the scope of this paper and will be pursued in a subsequent publication.

4.1 Rational dual basis functions

If rational basis functions are used, we define the dual basis as

$$\bar{R}_I = W \bar{N}_i \tag{21}$$

where W is the rational weight given in (8). Now

$$\int_{\hat{\Gamma}} \bar{R}_I R_J^s \, ds = \int_{\hat{\Gamma}} \bar{N}_I N_J^s \, ds = \delta_{IJ}. \tag{22}$$

4.2 Discretization

Over the slave interface we introduce the discretizations

$$\mathbf{u}^m = \sum_I N_I^m \left(\varphi(\xi^s) \right) \mathbf{d}_I^m \tag{23}$$

$$\mathbf{u}^s = \sum_I N_I^s(\xi^s) \mathbf{d}_I^s \tag{24}$$

$$\delta\mathbf{\Phi} = \sum_I \bar{N}_I(\xi^s) \, \delta\mathbf{\Phi}_I \tag{25}$$

where $\xi^s \in \hat{\Gamma}^s$ is a parametric position on the slave interface and $\varphi : \hat{\Gamma}^s \to \hat{\Gamma}^m$ is a compositional mapping defined to be

$$\varphi = (\mathbf{x}^m)^{-1} \circ \mathbf{x}^s \tag{26}$$

where $\mathbf{x}^s : \hat{\Omega}^s \to \Omega^s$ and $\mathbf{x}^m : \hat{\Omega}^m \to \Omega^m$ are the slave and master geometric mappings, respectively, as shown in Figure 2. Note that we say the master and slave parameterizations are matched if the mapping φ is linear, otherwise, we say the master and slave parameterizations are mismatched. In the mismatched case φ can be computed using the Newton-Raphson algorithm.

Note that discretizing (13c) and leveraging the biorthogonality property of the dual basis gives

$$\mathbf{d}^s = \mathbf{G}_{\bar{N},N^m} \mathbf{d}^m. \tag{27}$$

where

$$\mathbf{G}_{\bar{N},N^m} = \int_{\hat{\Gamma}} \bar{N}_I(\xi^s) N_J^m \left(\varphi(\xi^s) \right) \mathbf{I} ds \tag{28}$$

is a diagonal matrix.

The matrix form of (13) can be written as

$$\begin{bmatrix} \mathbf{K}^m & 0 & (\mathbf{K}^{\ell m})^{\mathrm{T}} \\ 0 & \mathbf{K}^s & -(\mathbf{K}^{\ell s})^{\mathrm{T}} \\ \mathbf{K}^{\ell m} & -\mathbf{K}^{\ell s} & 0 \end{bmatrix} \begin{bmatrix} \mathbf{d}^m \\ \mathbf{d}^s \\ \mathbf{d}^\ell \end{bmatrix} = \begin{bmatrix} \mathbf{f}^m \\ \mathbf{f}^s \\ 0 \end{bmatrix} \tag{29}$$

where $\mathbf{K}^m$ and $\mathbf{K}^s$ are standard patch-level stiffness matrices, $\mathbf{f}^m$ and $\mathbf{f}^s$ are the corresponding force vectors, and $\mathbf{K}^{\ell m}$ and $\mathbf{K}^{\ell s}$ are stiffness matrices with all entries equal to zero except for those related to the Ith Lagrange multiplier basis $\bar{N}_I$ and the Jth master and slave interface basis N_J^m and N_J^s, respectively. In other words, the nonzero entries of $\mathbf{K}^{\ell m}$ and $\mathbf{K}^{\ell s}$ can be written as

$$K^{\ell m}_{\bar{N}_I, N_J^m} = \int_{\hat{\Gamma}} \bar{N}_I N_J^m ds \tag{30}$$
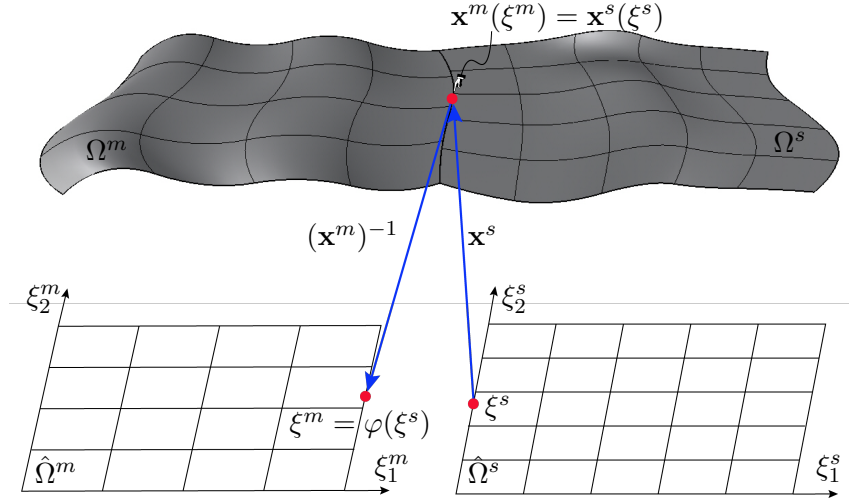
Figure 2: Slave and master geometric mappings, $\mathbf{x}^s$ and $\mathbf{x}^m$.

and

$$K^{\ell s}_{\bar{N}_I, N_J^s} = \int_{\hat{\Gamma}} \bar{N}_I N_J^s ds = \delta_{IJ}. \tag{31}$$

The displacement vectors $\mathbf{d}^m$ and $\mathbf{d}^s$ can be split such that

$$\mathbf{d}^m = \begin{bmatrix} \mathbf{d}_d^m \\ \mathbf{d}_c^m \end{bmatrix} \quad \text{and} \quad \mathbf{d}^s = \begin{bmatrix} \mathbf{d}_d^s \\ \mathbf{d}_c^s \end{bmatrix} \tag{32}$$

and the corresponding stiffness matrices $\mathbf{K}^m$, $\mathbf{K}^s$, $\mathbf{K}^{\ell m}$ and $\mathbf{K}^{\ell s}$ are

$$\mathbf{K}^m = \begin{bmatrix} \mathbf{K}_{dd}^m & \mathbf{K}_{dc}^m \\ \mathbf{K}_{cd}^m & \mathbf{K}_{cc}^m \end{bmatrix} \qquad \mathbf{K}^m = \begin{bmatrix} \mathbf{K}_{dd}^s & \mathbf{K}_{dc}^s \\ \mathbf{K}_{cd}^s & \mathbf{K}_{cc}^s \end{bmatrix} \qquad \mathbf{K}^{\ell m} = \begin{bmatrix} \mathbf{0} \\ \hat{\mathbf{K}}^{\ell m} \end{bmatrix}^{\mathrm{T}} \quad \text{and} \quad \mathbf{K}^{\ell s} = \begin{bmatrix} \mathbf{0} \\ \hat{\mathbf{K}}^{\ell s} \end{bmatrix}^{\mathrm{T}} \tag{33}$$

where the subscript d indicates the *distinct* degrees-of-freedom internal to each patch, and c indicates the degrees-of-freedom along the interface. The entries of $\hat{\mathbf{K}}^{\ell m}$ and $\hat{\mathbf{K}}^{\ell s}$ are defined in (30) and (31), respectively. Substituting (32) and (33), and the relation (27) between $\mathbf{d}_c^s$ and $\mathbf{d}_c^m$ into (29) allows us to statically condense the Lagrange multiplier coefficients $\mathbf{d}^\ell$ and the slave patch degrees-of-freedom $\mathbf{d}_c^s$ leading to the simplified system

$$\begin{bmatrix} \mathbf{K}_{dd}^m & \mathbf{K}_{dc}^m & 0 \\ \mathbf{K}_{cd}^m & \mathbf{K}_{cc}^m + (\mathbf{G}_{\bar{N}, N^m})^{\mathrm{T}} \mathbf{K}_{cc}^s \mathbf{G}_{\bar{N}, N^m} & (\mathbf{G}_{\bar{N}, N^m})^{\mathrm{T}} \mathbf{K}_{cd}^s \\ 0 & \mathbf{K}_{dc}^s \mathbf{G}_{\bar{N}, N^m} & \mathbf{K}_{dd}^s \end{bmatrix} \begin{bmatrix} \mathbf{d}_d^m \\ \mathbf{d}_c^m \\ \mathbf{d}_d^s \end{bmatrix} = \begin{bmatrix} \mathbf{f}_d^m \\ \mathbf{f}_c^m + (\mathbf{G}_{\bar{N}, N^m})^{\mathrm{T}} \mathbf{f}_c^s \\ \mathbf{f}_d^s \end{bmatrix}. \tag{34}$$

Note that all problems in this paper are solved with this simplified system of equations rather than (29).

If the interface energy term in (12) is defined on the physical domain instead of the parametric domain the dual basis must be defined as

$$\bar{\mathbf{N}}^e = \frac{1}{|\mathbf{J}|} \operatorname{diag}(\boldsymbol{\omega}^e)(\mathbf{R}^e)^T (\mathbf{G}_{B,B}^e)^{-1} \mathbf{B}^{e,s} \tag{35}$$

$$= \frac{1}{|\mathbf{J}|} \mathbf{D}^e \mathbf{B}^{e,s} \tag{36}$$

where $\mathbf{J}$ is the Jacobian of the geometric mapping $\mathbf{x}^s$.

9

4.3 Refinement of the dual basis

If the master and slave parameterizations are matched, the underlying basis have the same degrees, and the knots along the master interface are contained in the slave interface the interface constraint (13c) is imposed exactly. In this case, $\mathbf{G}_{\bar{N},N^m}$ is then a standard spline refinement operator. In any case, the approximation can be improved without adding additional degrees-of-freedom to the global system by refining the slave interface and dual basis. We highlight that if the slave interface is refined, quadrature error accumulates if the new lines of reduced continuity in the slave interface are not accounted for in the element domains $\hat{\Omega}^{s,e}$ which touch the slave interface. For example, in Figure 3, two quadratic, linearly parameterized B-spline patches meet at a common interface. A refinement is performed in which all knots in the master interface which are not already present in the slave interface are added, i.e., the knot $\frac{1}{2}$ is inserted into the slave interface. To properly account for the new line of reduced continuity in the slave interface element e_2, it is subdivided into two elements e_{21} and e_{22} and quadrature is performed on both subelements. The nodes whose basis functions are supported by element e_{21} are depicted in Figure 3. Note that the method is stable under refinement since dual basis refinement adds the same number of Lagrange multiplier degrees-of-freedom as slave interface degrees-of-freedom. As a result, the matrix $\mathbf{K}^{\ell s}$ in (29) has full row rank.

For the case where many mismatched patches are required to define a geometric domain more advanced local refinement schemes could be utilized such as those commonly used for analysis-suitable T-splines [37]. In fact, the process described in Figure 3 for inserting master knots into the slave interface is a particular type of local T-spline knot insertion. For most of cases considered in this paper, two global uniform refinements of the slave interface was enough to recover optimal higher-order convergence rates.
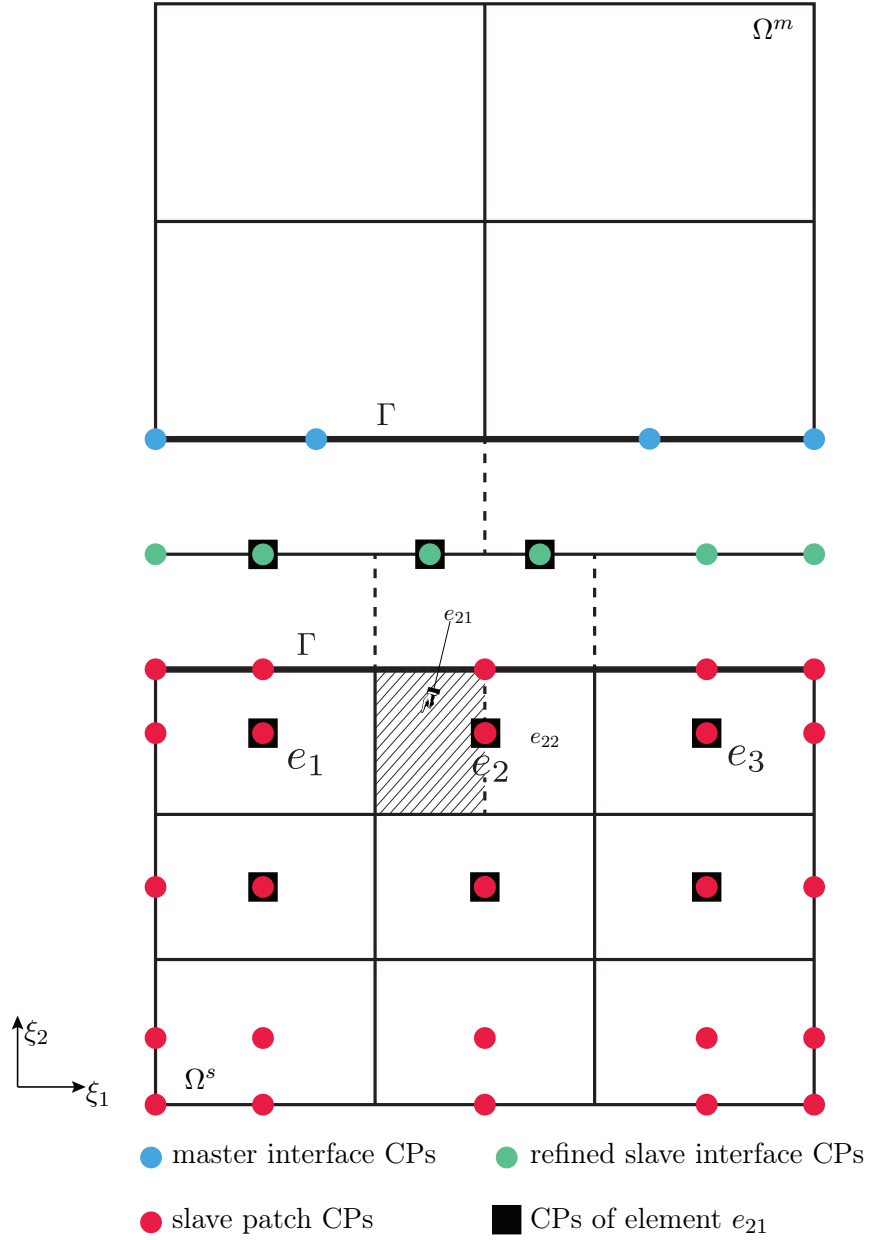
Figure 3: Refinement of a slave interface and corresponding control points (CPs).

5 Weakly continuous geometry

Since the weak continuity constraint is defined on the parametric domain of the slave interface Bézier dual mortaring can also be viewed as an isogeometric design methodology for building multi-patch geometry where the weak continuity constraint is built into the space spanned by the geometric basis. In this case, weak geometric compatibility is preserved for any choice of control points and the dual mortaring no longer needs to be incorporated into the finite element assembly algorithm. To build the weak continuity constraint into the element extraction operators we start by noticing that

$$\mathbf{N}^m = (\mathbf{G}_{\bar{N},N^m})^{\mathrm{T}}\mathbf{N}^s \tag{37}$$

which can be localized to each element on the interface

$$\mathbf{N}^{m,e} = (\mathbf{G}^e_{\bar{N},N^m})^{\mathrm{T}}\mathbf{R}^e\mathbf{B}^{e,s} \tag{38}$$

$$= \tilde{\mathbf{R}}^e\mathbf{B}^{e,s} \tag{39}$$

where $\tilde{\mathbf{R}}^e$ is called a weakly continuous element extraction operator. Since

$$\tilde{\mathbf{R}}^e = (\mathbf{G}^e_{\bar{N},N^m})^{\mathrm{T}}\mathbf{R}^e \tag{40}$$

it is clear that each row of $\tilde{\mathbf{R}}^e$ (which corresponds to a master basis function) is formed by taking a linear combination of rows in $\mathbf{R}^e$ (which correspond to slave basis functions) where the weighting in the linear combination comes from the columns of $\mathbf{G}^e_{\bar{N},N^m}$.

If the slave interface is refined, then (37) can be written as

$$\mathbf{N}^m = (\mathbf{G}_{\bar{N}^r,N^m})^{\mathrm{T}}\mathbf{N}^r \tag{41}$$

where $\mathbf{N}^r$ is the refined slave interface basis vector. Similarly, (38) can be written as

$$\mathbf{N}^{m,e} = (\mathbf{G}^e_{\bar{N}^r,N^m})^{\mathrm{T}}\mathbf{R}^{e,r}\mathbf{B}^{e,r} = (\mathbf{G}^e_{\bar{N}^r,N^m})^{\mathrm{T}}\mathbf{R}^{e,r}\mathbf{M}^{-\mathrm{T}}\mathbf{B}^{e,s} \tag{42}$$

where $\mathbf{R}^{e,r}$ is the standard element extraction operator defined on the refined slave interface, and $\mathbf{M}$ is the Bernstein basis transformation matrix defined in (3). Therefore, the weakly continuous element extraction operator can be written as

$$\tilde{\mathbf{R}}^e = (\mathbf{G}^e_{\bar{N}^r,N^m})^{\mathrm{T}}\mathbf{R}^{e,r}\mathbf{M}^{-\mathrm{T}}. \tag{43}$$

Figure 4 shows the action of (43) for the interface element e_{21} in Figure 3 and the resulting weakly continuous two-dimensional basis functions along the interface are shown in Figure 5. The full expressions for the weakly continuous element extraction operators $\tilde{\mathbf{R}}^e$ are given in the A.

(a) Master interface basis (top) and refined slave interface basis (bottom).

(b) Transformation of basis functions for element e_{21}.
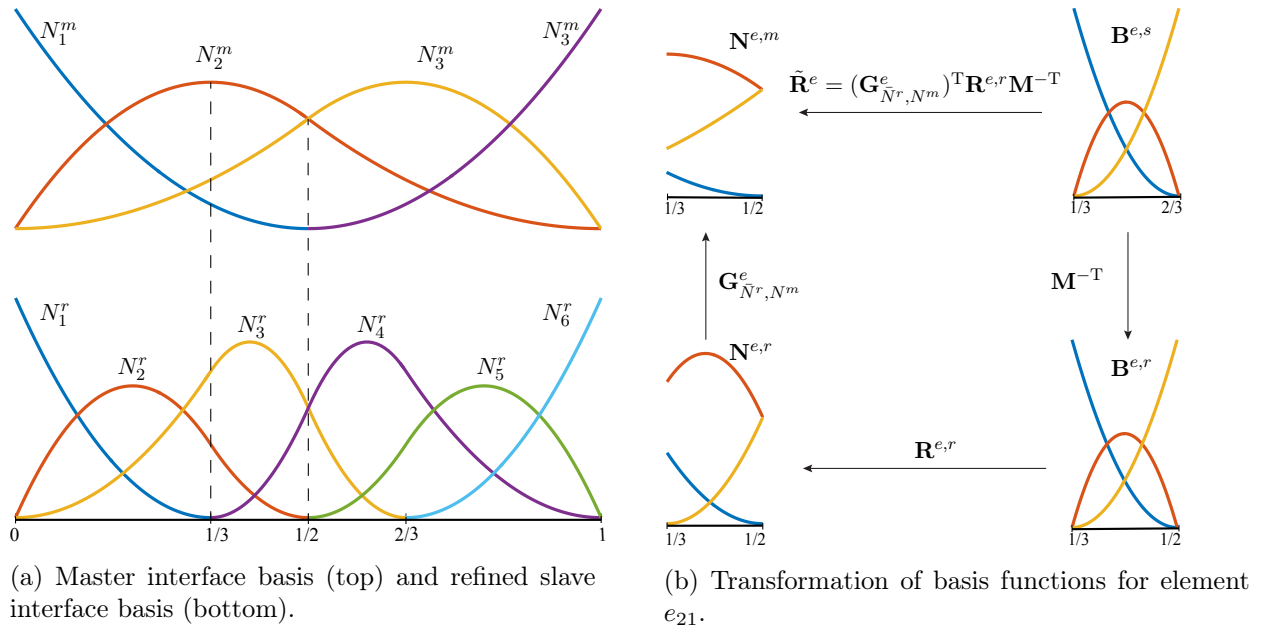
Figure 4: Construction of a refined interface extraction operator for element e_{21} from Figure 3.
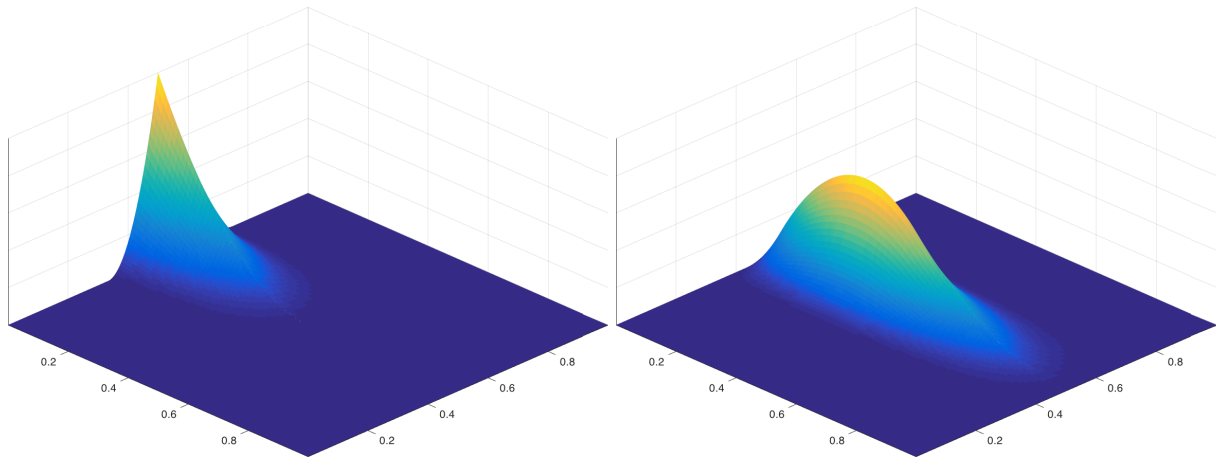
(a) First interface basis.

(b) Second interface basis.
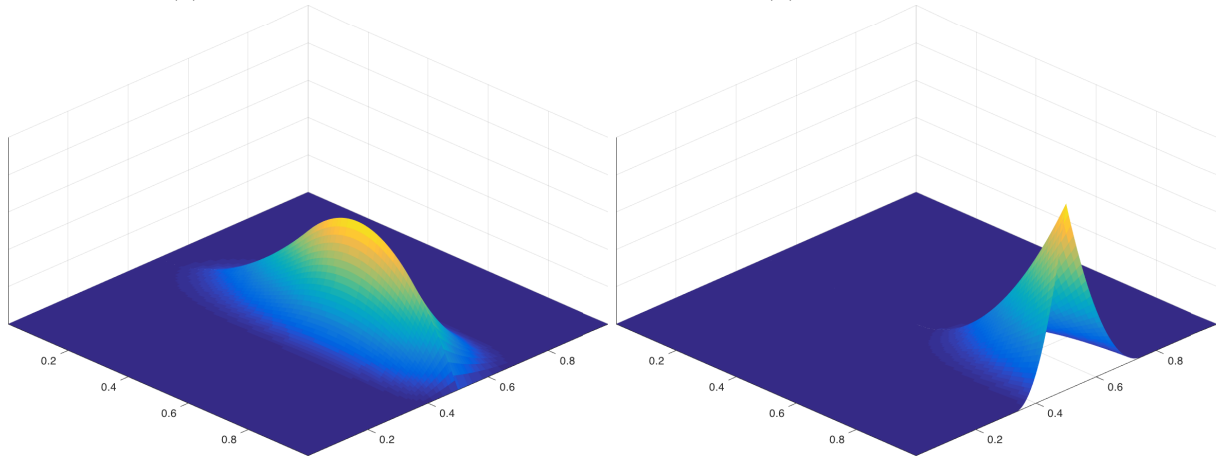
(c) Third interface basis.

(d) Fourth interface basis.

Figure 5: Weakly continuous basis functions along an interface corresponding to the mesh shown in Figure 3.

6 Numerical results

We evaluate the performance of the Bézier dual mortar method on several challenging benchmark problems. In all cases, dual basis refinement is employed where, during the first step of refinement, the master knots are projected into the slave interface. Subsequent refinement then utilizes uniform element subdivision of the slave interface. To avoid the well-known mortar integral error in calculating $\mathbf{G}_{\bar{N},N^m}$ in (28) when no refinement of the dual basis is employed, the master knots are still projected into the slave interface and the integration is performed on the combined knot intervals as described in [14]. Note that the first step of refinement might generate subelements with high aspect ratios if the projected master knots are too close to the original slave interface knots. These knots can be easily filtered out. In this work, if the parametric interval of a slave subelement is less than $\frac{1}{20}^{th}$ of the original parametric interval the projected master knot is ignored. Note that during the first step of refinement, uniform subdivision could also be employed. However, a small error would be incurred due to the integration error in calculating $\mathbf{G}_{\bar{N},N^m}$. However, for complex parameterizations in three-dimensions (including volumetric parameterizations) this error may be an acceptable trade-off to avoid an expensive combined master/slave segmentation step. We compare our method to a global dual mortar method [10, 14], where the global dual basis is computed using L^2 projection.

6.1 A manufactured solution on a square domain

We first solve the Laplace equation, $-\Delta u = 0$, on the square domain, $\Omega = (0,1) \times (0,1)$. The domain is modeled with two maximally smooth quadratic B-spline patches where the left patch is the master and the right patch is the slave as shown in Figure 6. Two different boundary conditions, shown in Figure 6a and b, are considered to demonstrate that, in contrast to the global dual mortar method, the Bézier dual mortar method does not suffer from the so-called crosspoint problem [14, 15]. This superior performance is due to the locality of the dual basis functions. Both boundary conditions satisfy the manufactured solution, $u(x,y) = \sin(\pi y)\sinh(\pi x)$. The ratio of master to slave element size is initially chosen to be $2:3$. The master and slave interface boundaries are matched but the underlying meshes are nonconforming.

The sparsity patterns for the stiffness matrices for the proposed method, a global dual mortar method, and a standard conforming method are shown in Figure 7a, 7b, and 7c, respectively, after four applications of uniform global refinement. It is clear that the proposed method generates a sparse stiffness matrix with only a slight increase in bandwidth when compared to a conforming method.

We first present results for the boundary condition shown in Figure 6a. The convergence rates of the displacement error in the L^2-norm for several different degrees are shown in Figure 8a. The proposed approach is compared to a global dual mortar method. As can be seen, the global dual mortar method only gets optimal rates for $p = 1$, and for $p = 2, 3, 4$ the convergence rates are 2, which is suboptimal. This reduction in the rates can be attributed to the crosspoint problem [14, 15]. In other words, the Lagrange multiplier space is bigger than the primal space due to the crosspoint, which, in this case, corresponds to the points where the interface and Dirichlet boundary conditions intersect. As a result, inf-sup stability is lost. *Without refinement of the dual basis*, the proposed method achieves optimal rates for $p = 1$, and slightly deteriorated rates for $p = 2$. For $p = 3, 4$, the convergence rates are reduced but still converge faster than the global dual mortar method. To demonstrate the insensitivity of the method to master and slave selection, we change the mesh ratio to $m:s = 3:2$. The convergence rates are shown in Figure 8b. As can be seen, the convergence rates are close to the previous case, $m:s = 2:3$.

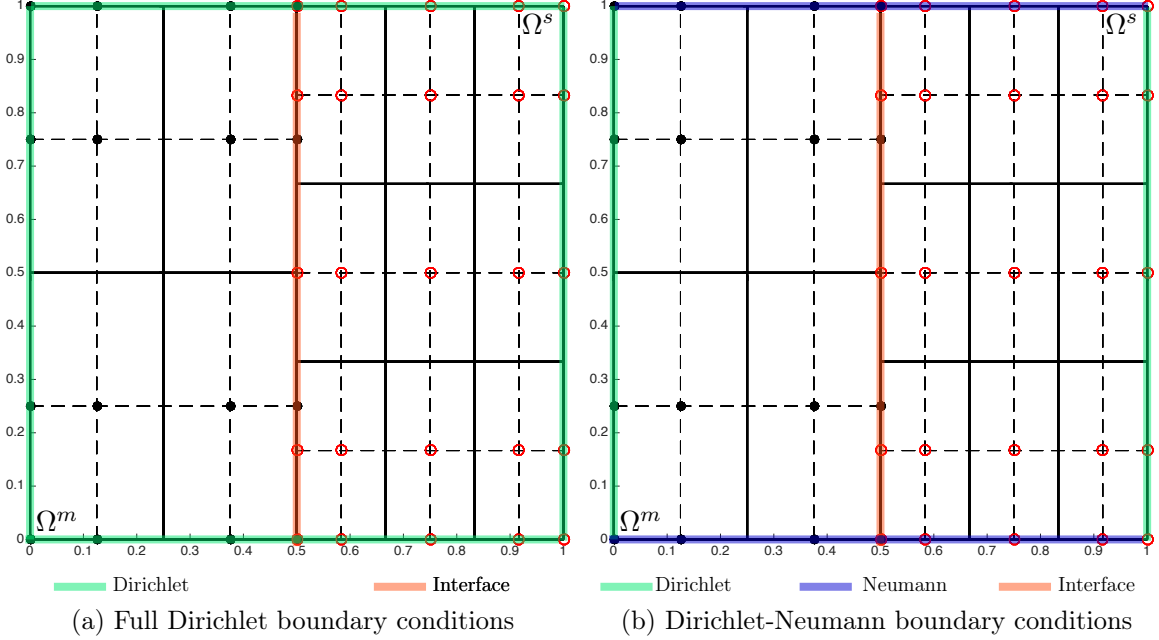(a) Full Dirichlet boundary conditions   (b) Dirichlet-Neumann boundary conditions

Figure 6: Two quadratic maximally smooth nonconforming B-spline patches.

We now refine the proposed dual space to improve the accuracy. The convergence rates are shown in Figure 9. As expected, with one refinement of the interface dual basis the proposed method obtains optimal convergence rates for all degrees $p = 1, 2, 3$, and 4 for both mesh ratios $m : s = 2 : 3$ and $m : s = 3 : 2$.

The second boundary condition case, shown in Figure 6b, allows for a comparison of the proposed method with the global dual method without crosspoint pollution. As shown in Figure 10, the optimality of the global dual mortar method can be observed for this case, while the proposed method behaves in a similar fashion as in the first full Dirichlet boundary condition case. Again, with one refinement, the Bézier dual mortar method obtains optimal rates as shown in Figure 11. This demonstrates that the proposed method is relatively insensitive to crosspoint pollution. This superior behavior can be attributed to the locality of the dual basis. The reduced rates in the proposed method without refinement is due to the lack of higher-order polynomial reproduction in the dual basis.

We next investigate the impact of mismatched parameterizations on the results. Mismatched parameterizations can be created by perturbing the position of the control points along the master and/or slave interfaces. To avoid crosspoint pollution we only consider the Dirichlet-Neumann boundary condition case. The convergence results for mesh ratio $m : s = 2 : 3$ without refinement are shown in Figure 12. Again, the global dual mortar method obtains the optimal rates for $p = 2, 3$ and 4. Without refinement of the dual basis, the Bézier dual mortar method behaves in a manner which is similar to the matched parameterization case. To improve solution behavior we refine the dual basis. The resulting convergence rates are shown in Figure 13. Since the geometric mapping is no longer linear, the continuity constraint (13c) cannot be imposed exactly by refining the dual basis once. Therefore, optimal rates cannot be achieved. However, we can improve the accuracy by simply refining the dual space additional times. As shown in Figure 13, for $p = 2, 3$, uniformly refining the dual space once recovers optimal rates and refining twice recovers optimal rate for $p = 4$. Recall that regardless of how many times the dual space is refined the number of global degrees-of-freedom remains fixed.

(a) The proposed method   (b) A global dual mortar method   (c) A conforming method
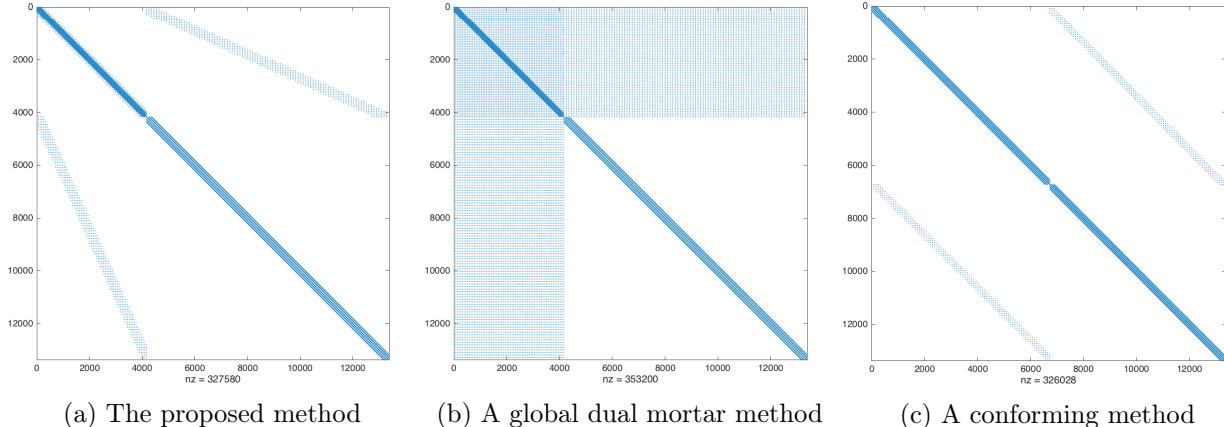
Figure 7: Stiffness matrix sparsity patterns for (a) the proposed method, (b) a global dual mortar method, and (c) a standard conforming method. The nonconforming examples (i.e., (a) and (b)) are generated from nonconforming meshes after uniformly refining the initial mesh shown in Figure 6 four times. The resulting mesh has 13862 nodes. The conforming example in (c) is generated from a mesh with 13860 nodes.

We next study the case where both the parameterizations and degrees are mismatched. In this case, the degree of the master patch is one order higher than the slave patch. As shown in Figure 14, without refinement of the dual basis, optimal rates are only obtained for the case $p^m = 3$, $p^s = 2$ and mesh ratio $m : s = 2 : 3$. Note that the optimal rates are bounded by the lower degree among the different patches. As expected, refining the dual basis improves its approximation ability. Therefore, optimal rates are obtained for $p^m = 4$, and $p^s = 3$ with both mesh ratios, $m : s = 2 : 3$ and $m : s = 3 : 2$.

6.2   A manufactured solution on an annular domain

We now solve the Poisson equation, $-\Delta u = f$, on the annular domain, $\Omega = \left\{ (r, \phi) \,|\, 0.4 \leq r \leq 4, \pi/2 \leq \phi \leq \pi \right\}$. This example tests the effectiveness of rational dual basis functions. The domain is composed of two NURBS patches as shown in Figure 15. The internal force and the boundary conditions correspond to the manufactured solution, $u(x, y) = \sin(\pi x) \sin(\pi y)$. As shown in Figure 15, there are no crosspoints in this problem. Note that we only consider matched parameterizations in this example.

The convergence rates in the L^2-norm of the displacement are shown in Figure 16 for $p = 2, 3, 4$, without refining the dual basis. As can be seen, the global dual mortar method achieves the optimal rates for all degrees and mesh ratios $m : s = 2 : 3$ and $m : s = 3 : 2$. The proposed method achieves the optimal rates for $p = 2, 3$ and $m : s = 2 : 3$, and slightly deteriorated convergence rate for $p = 4$. For mesh ratio $m : s = 3 : 2$, the proposed method experiences reduced convergence rates for $p = 3, 4$. However, one refinement recovers optimal rates for $p = 4$ with mesh ratio $m : s = 2 : 3$, and $p = 3$ and 4 with mesh ratio $m : s = 3 : 2$, as shown in Figure 17.

We next investigate mismatched degrees. For degrees $p^m = p^s - 1$ and mesh ratio $m : s = 3 : 2$, the convergence rates are shown in Figure 18a. In this case, the convergence behavior is similar to the matched degree case shown in Figure 17. Since the degree of the slave patch is higher than the master patch, the master interface knots are projected into the slave interface with enough repeated knots to match the lower smoothness of the master interface. This results in nested spaces and optimal rates are recovered. For degrees $p^m = p^s + 1$, nesting of spaces is not possible but, as can

be seen in Figure 18b, refining the dual basis twice recovers the optimal rates.
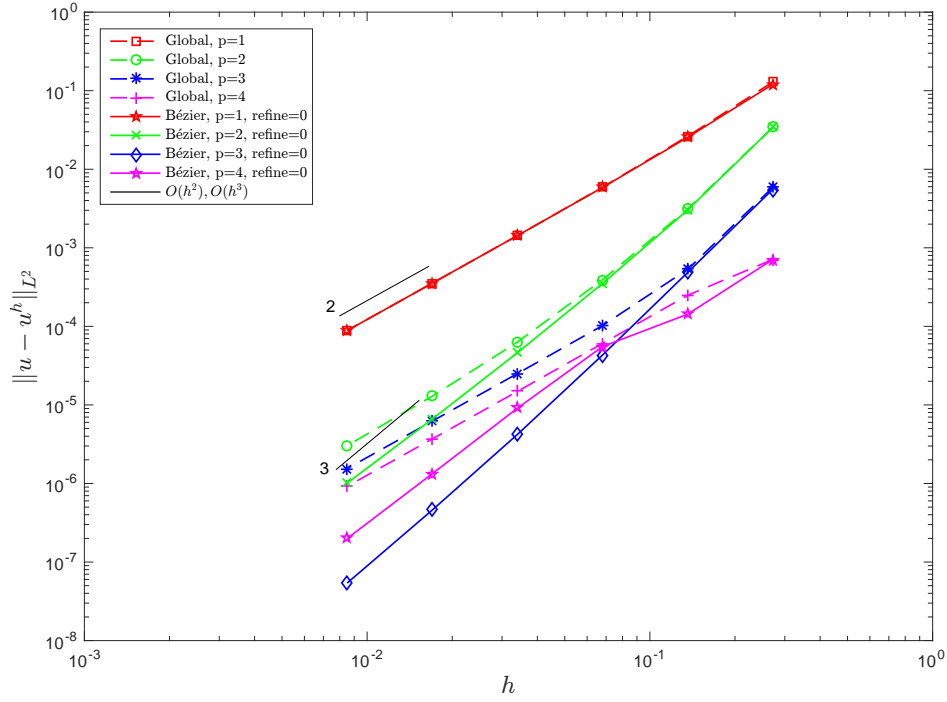
(a) Master/slave mesh ratio, $m : s = 2 : 3$
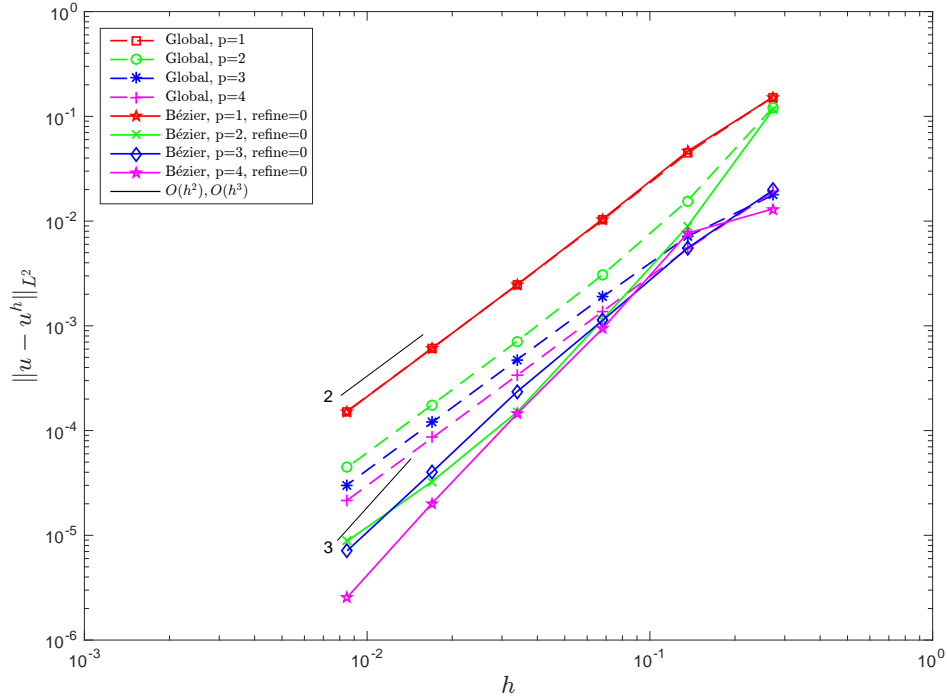
(b) Master/slave mesh ration, $m : s = 3 : 2$

Figure 8: Convergence rates for a square domain with two non-conforming patches, full Dirichlet boundary conditions (see Figure 6a) and matched parameterizations.
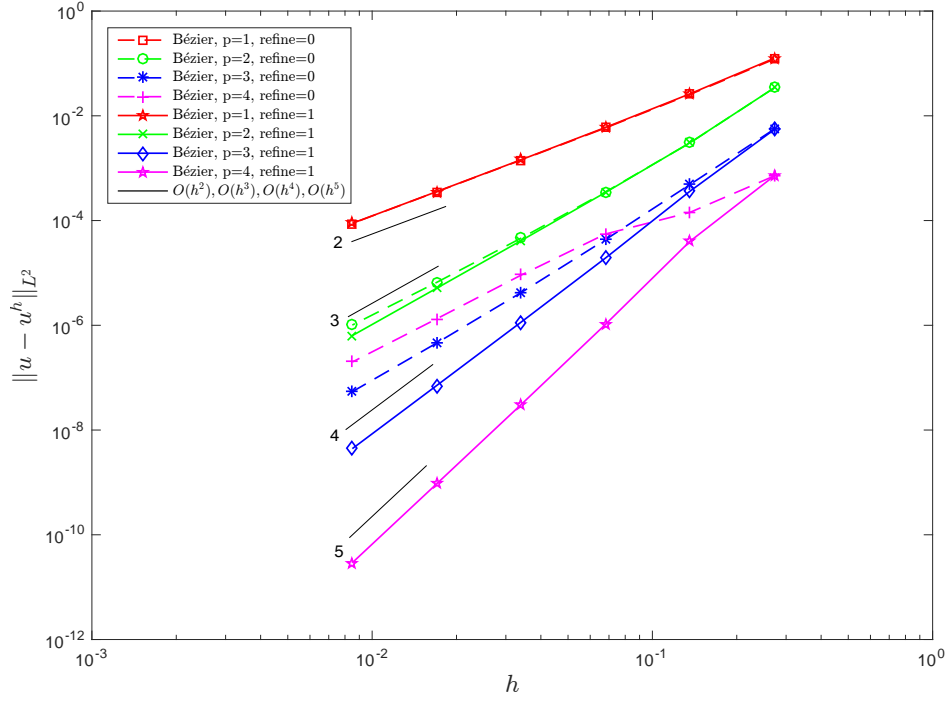
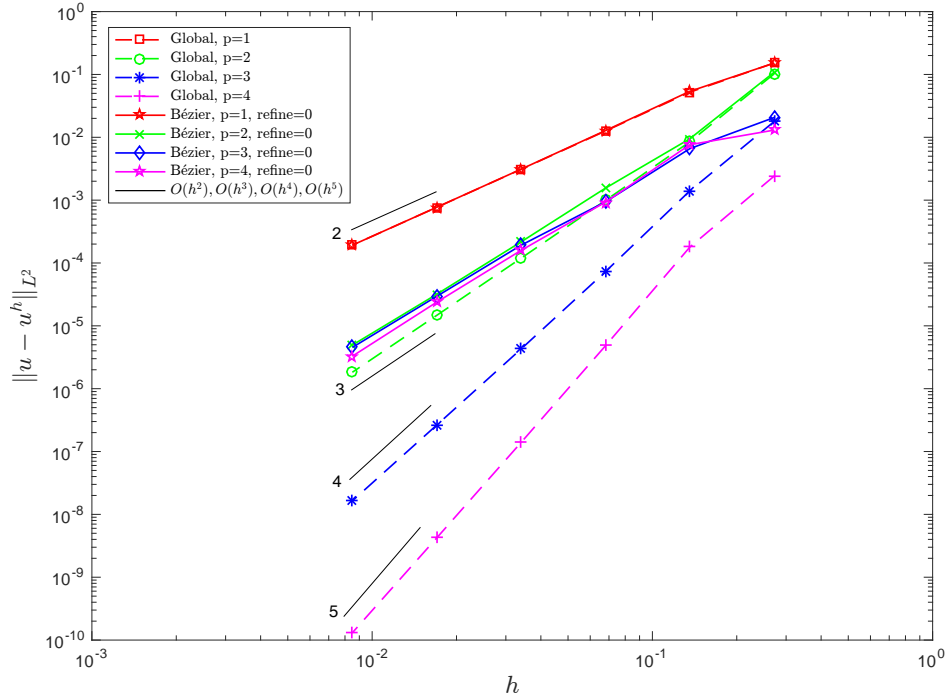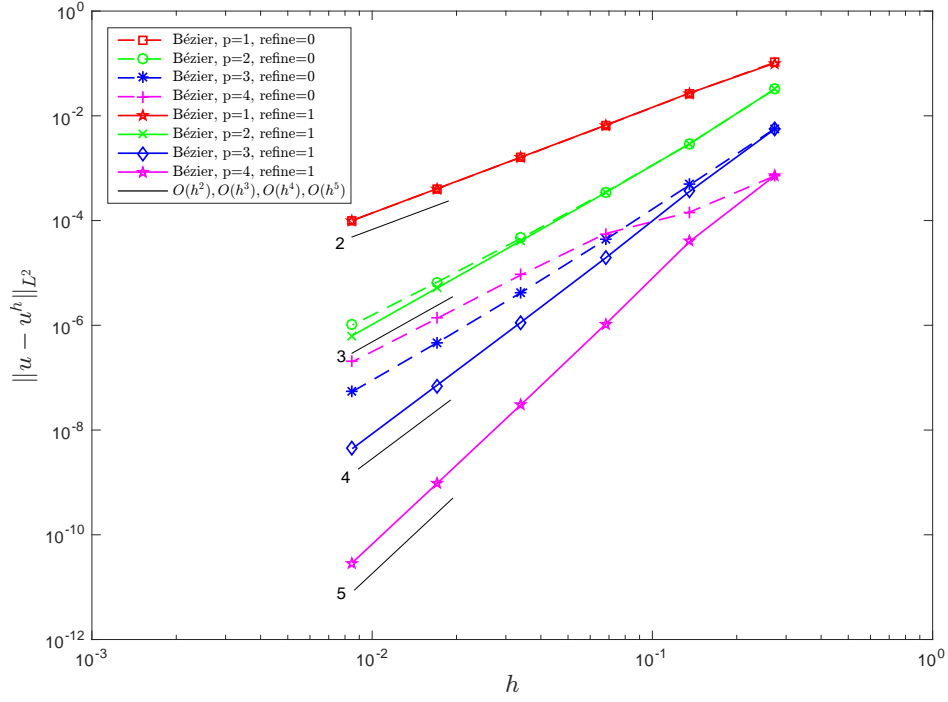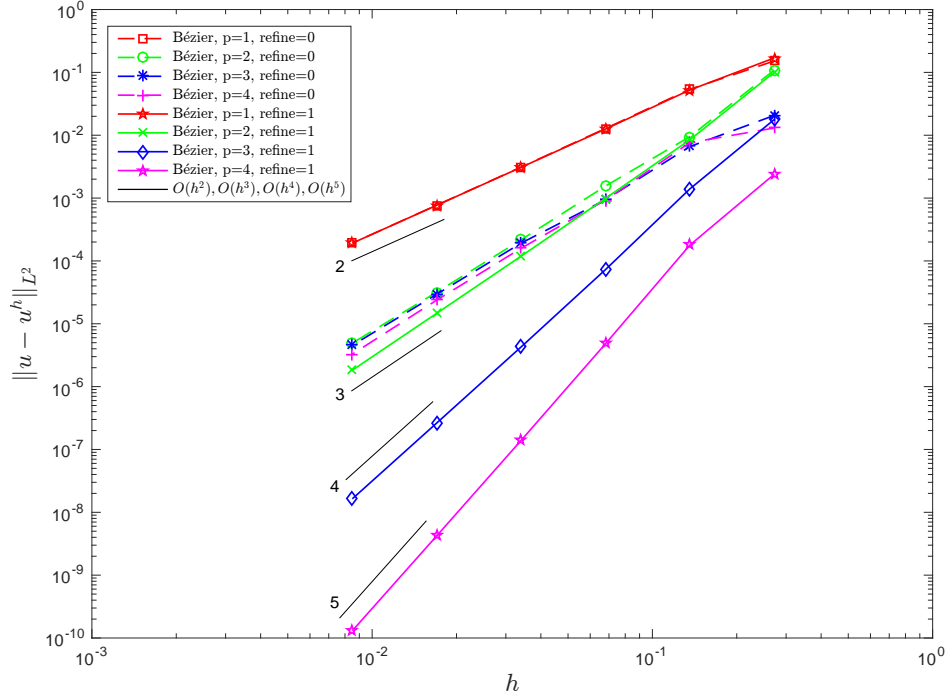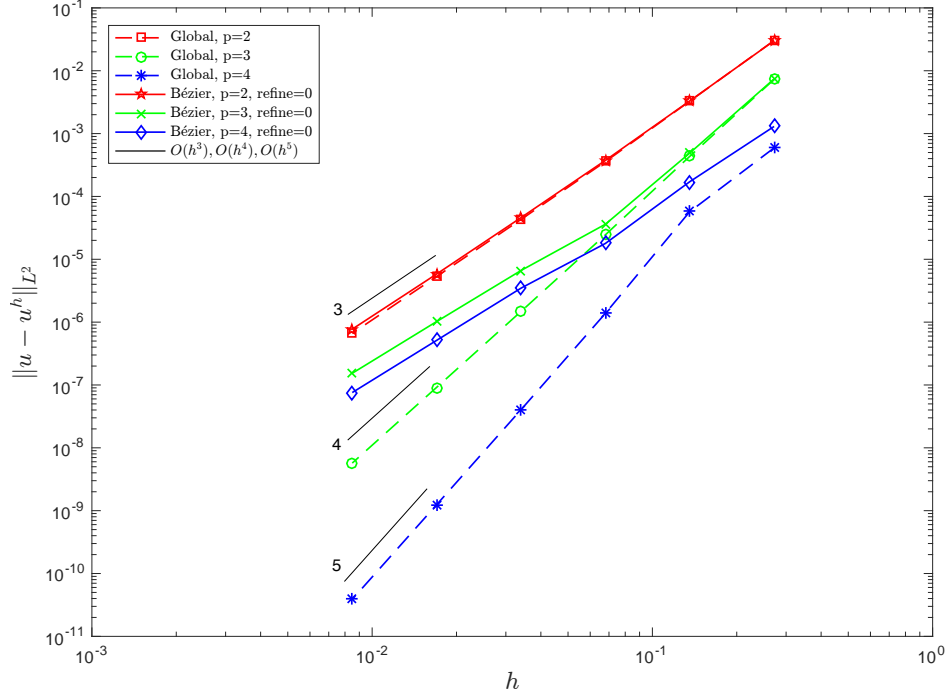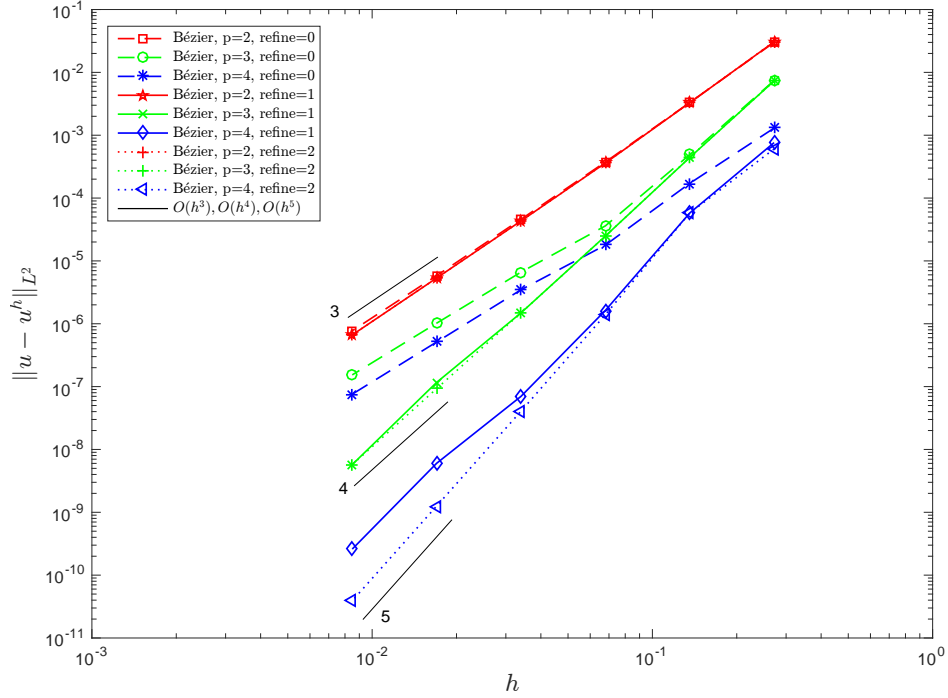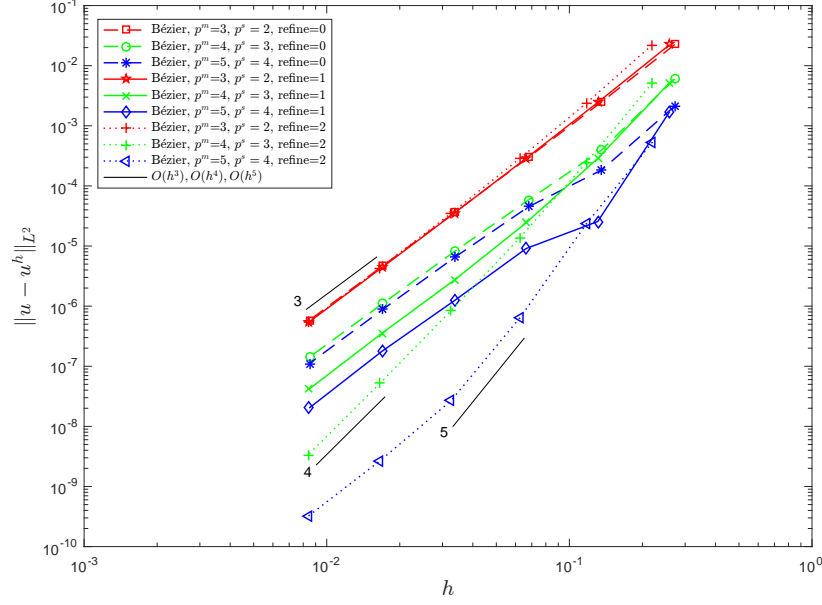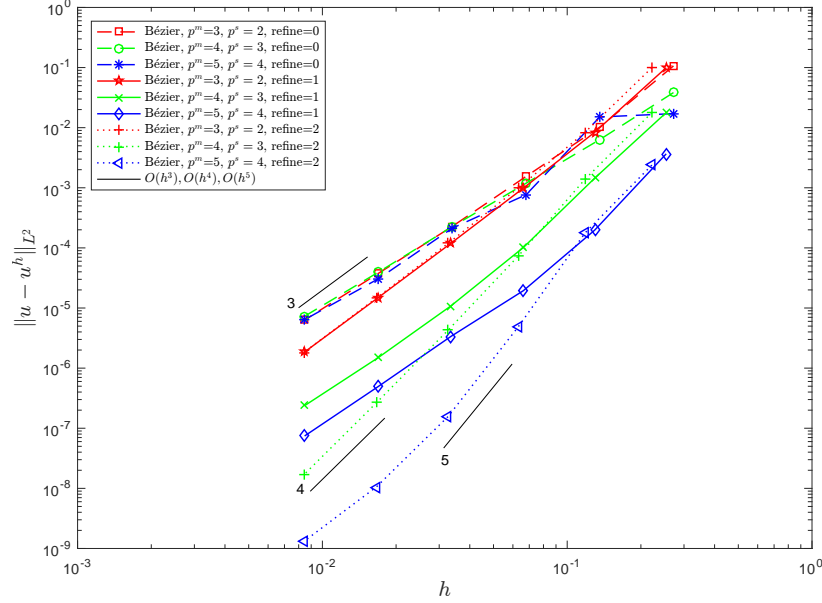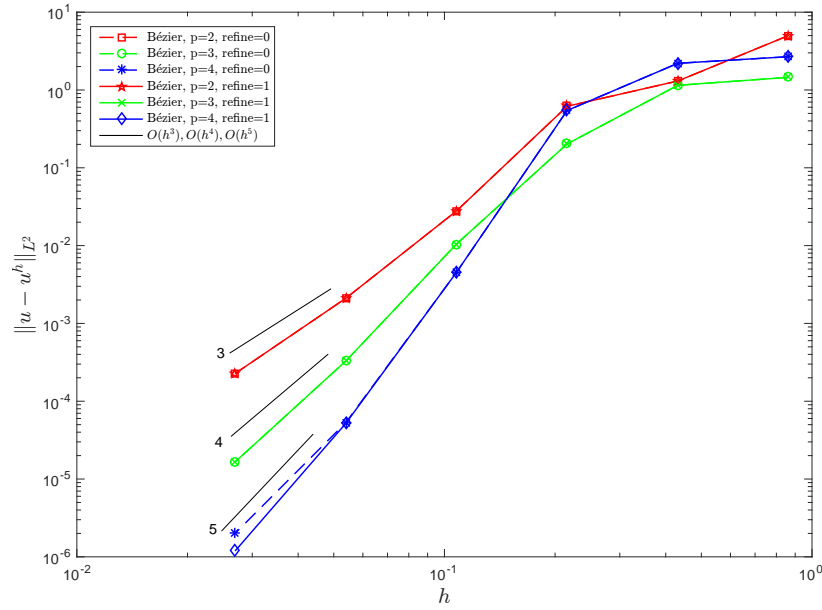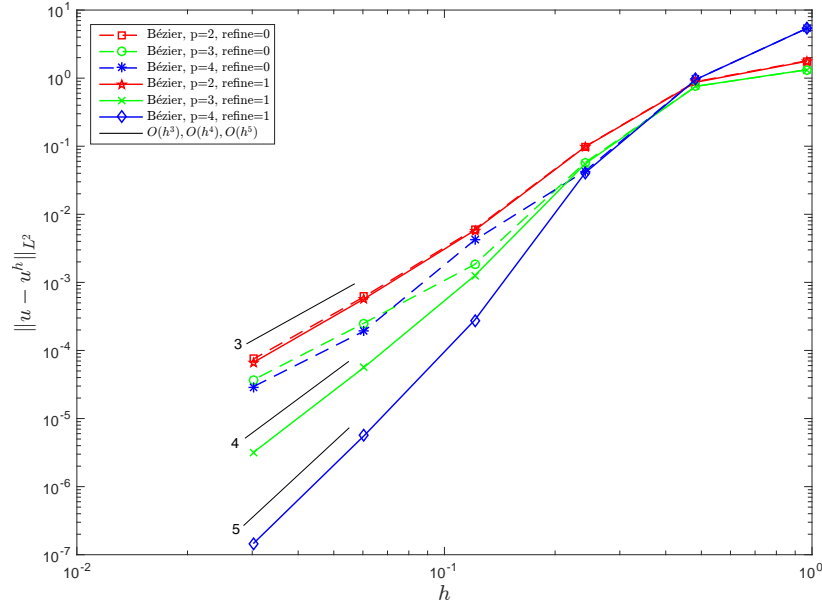(a) Master/slave mesh ratio, $m : s = 2 : 3$
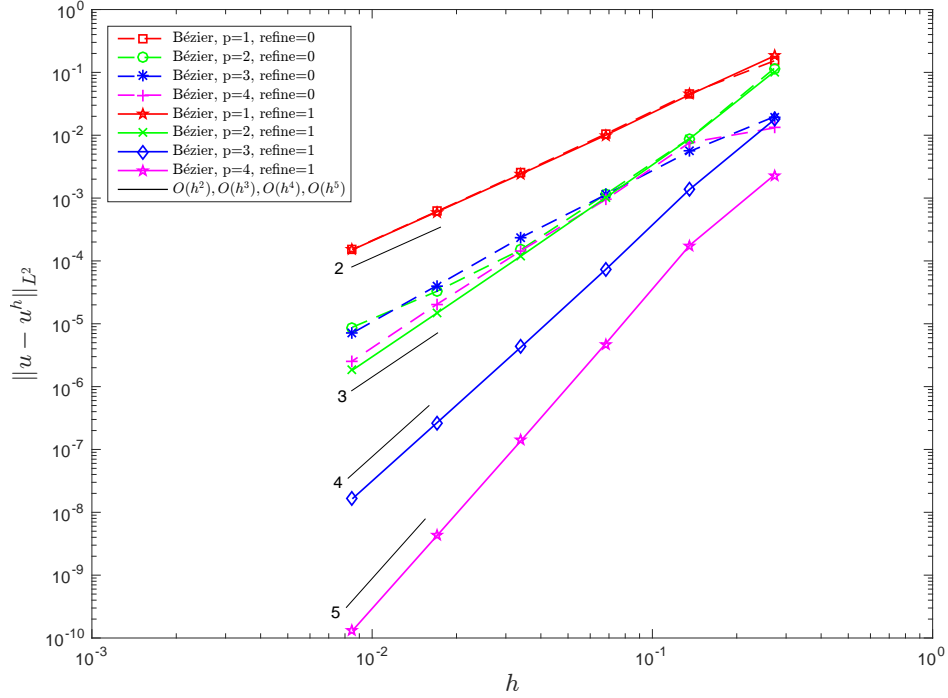
(b) Master/slave mesh ratio, $m : s = 3 : 2$

Figure 9: Convergence rates for a square domain with two non-conforming patches, full Dirichlet boundary conditions (see Figure 6a) and matched parameterizations where the dual space is refined n times, $n = 0, 1$.
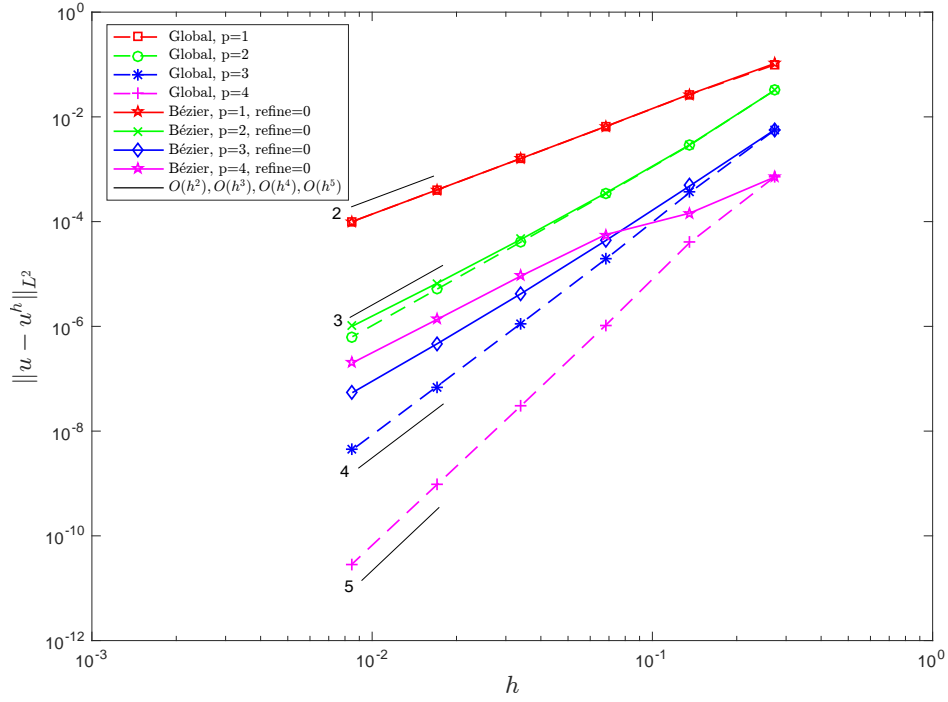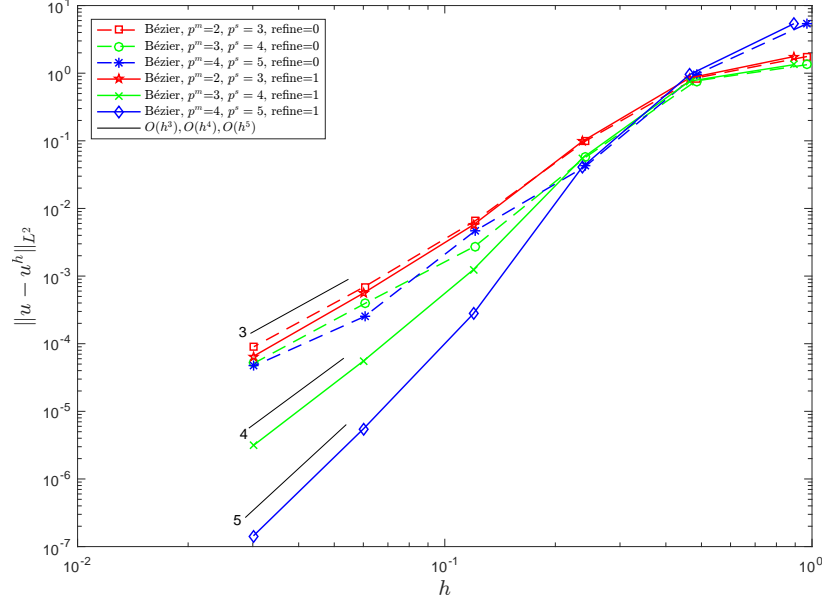
(a) Master/slave mesh ratio, $m : s = 2 : 3$

(b) Master/slave mesh ratio, $m : s = 3 : 2$

Figure 10: Convergence rates for a square domain with two non-conforming patches, Dirichlet-Neumann boundary conditions (see Figure 6b), and matched parameterizations.
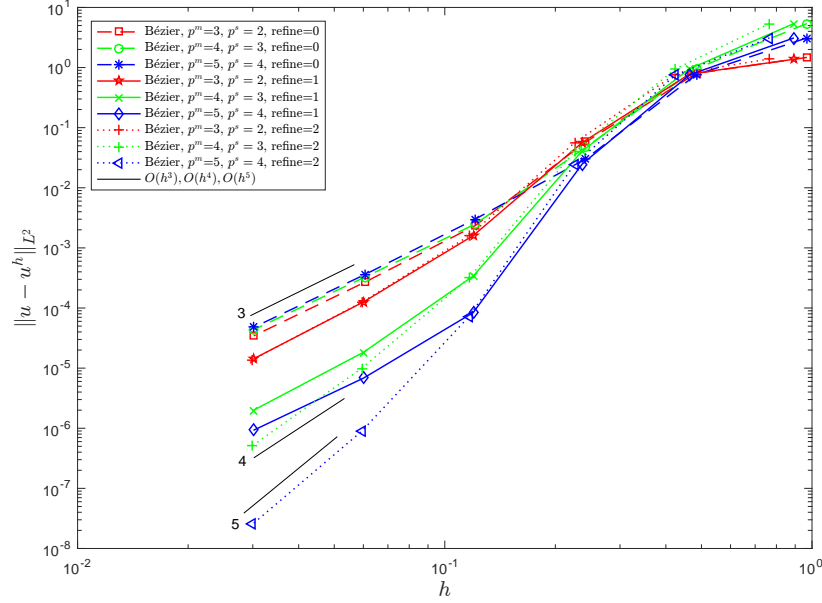
(a) Master/slave mesh ratio, $m : s = 2 : 3$

(b) Master/slave mesh ratio, $m : s = 3 : 2$

Figure 11: Convergence rates for a square domain with two non-conforming patches, Dirichlet-Neumann boundary conditions (see Figure 6b), matched parameterizations where the dual space is refined n times, $n = 0, 1$.

Figure 12: Convergence rates for a square domain with two non-conforming patches, Dirichlet-Neumann boundary conditions (see Figure 6b) and mismatched parameterizations, master/slave mesh ratio, $m : s = 2 : 3$.

Figure 13: Convergence rates for a square domain with two non-conforming patches, Dirichlet-Neumann boundary conditions (see Figure 6b) and mismatched parameterizations where the dual space is refined n times, $n = 0, 1, 2$, master/slave mesh ratio, $m : s = 2 : 3$.

(a) Master/slave mesh ratio, $m : s = 2 : 3$

(b) Master/slave mesh ratio, $m : s = 3 : 2$

Figure 14: Convergence rates for a square domain with two non-conforming patches, Dirichlet-Neumann boundary conditions (see Figure 6b), mismatched parameterizations and degrees $p^m = p^s + 1$, where the dual space is refined n times, $n = 0, 1, 2$.
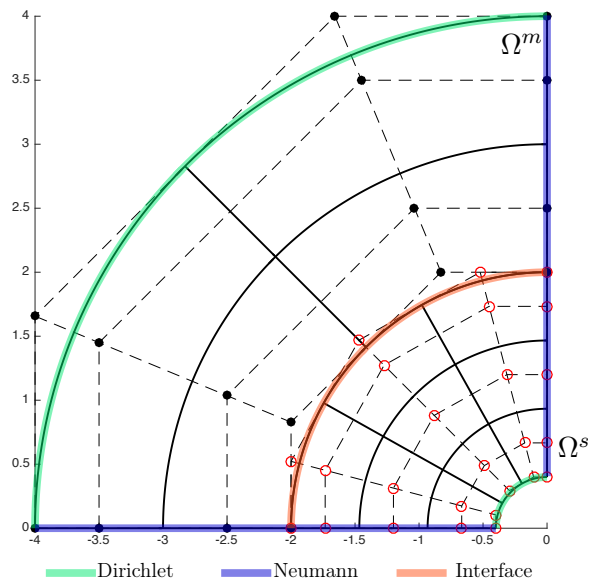
Figure 15: An annular domain composed of two quadratic nonconforming NURBS patches.
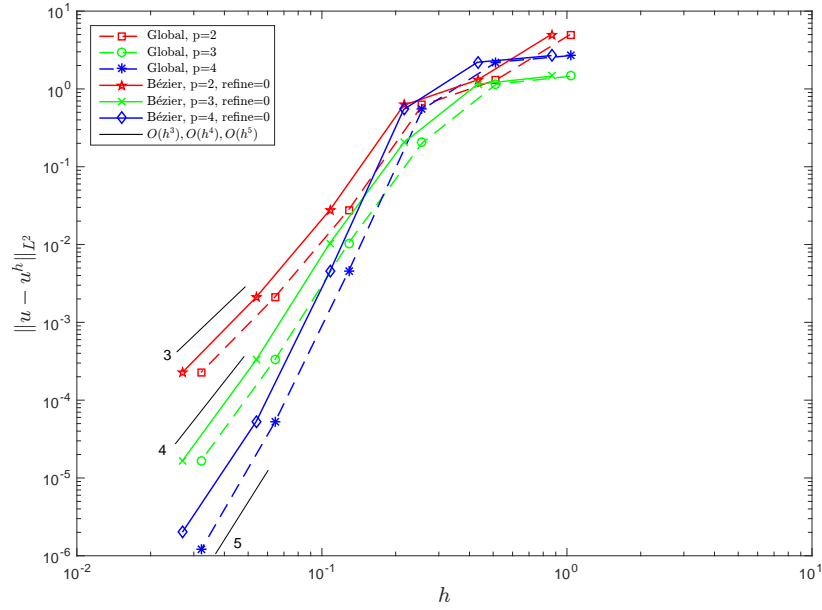
t

(a) Master/slave mesh ratio, $m : s = 2 : 3$
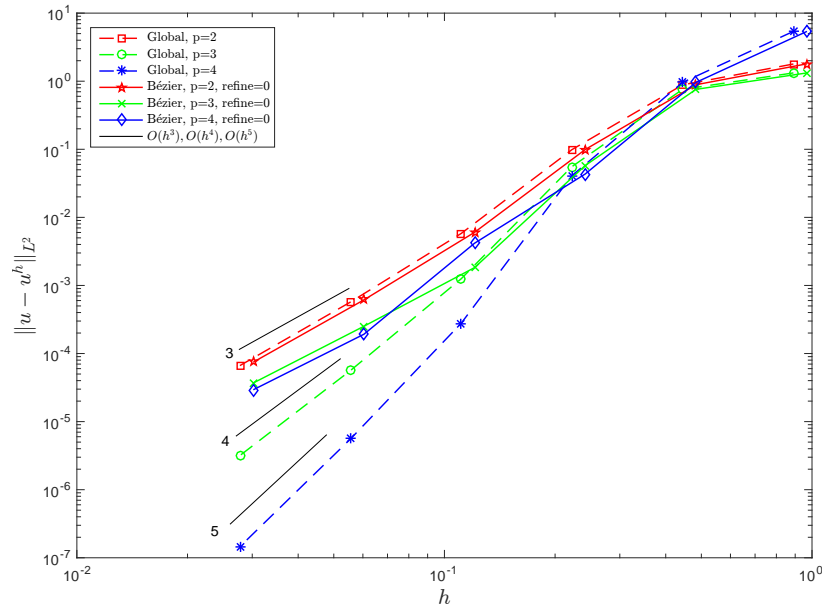
(b) Master/slave mesh ratio, $m : s = 3 : 2$

Figure 16: Convergence rates for an annular domain with two non-conforming NURBS patches, Dirichlet-Neumann boundary conditions (see Figure 15) and matched parameterizations.

(a) Master/slave mesh ratio, $m : s = 2 : 3$

(b) Master/slave mesh ratio, $m : s = 3 : 2$

Figure 17: Convergence rates for an annular domain with two non-conforming NURBS patches, Dirichlet-Neumann boundary conditions (see Figure 15) and refined matched parameterizations.

(a) Degree pair, $p^m = p^s - 1$

(b) Degree pair, $p^m = p^s + 1$

Figure 18: Convergence rates for an annular domain with two non-conforming NURBS patches, Dirichlet-Neumann boundary conditions (see Figure 15), matched parameterizations and mismatched degrees, master/slave mesh ratio $m : s = 3 : 2$.

6.3 Infinite elastic plate with a circular hole
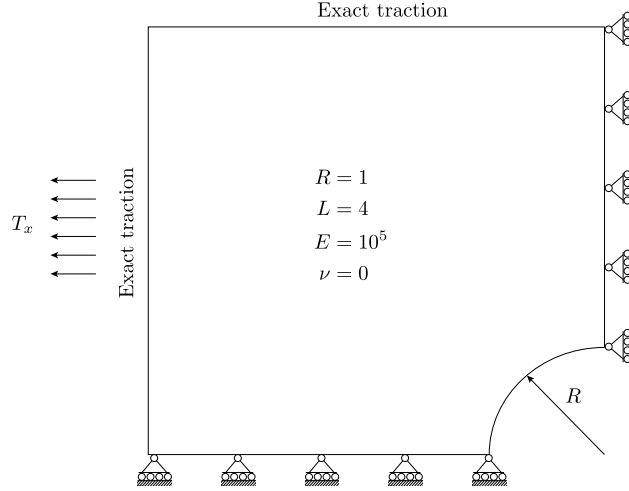
Figure 19: A schematic for the infinite elastic plate with a circular hole benchmark.

We next simulate the classical infinite elastic plate with a circular hole benchmark problem. In this case, we apply a constant traction in the x-direction at infinity. Due to symmetry, only one quarter of the plate is modeled as shown in Figure 19, where T_x is the traction, R is the radius of the hole, L is the length of each side of the plate, E is Young's modulus, and ν is Poisson's ratio. An analytical solution to this problem can be found in [2] and is reproduced here for completeness

$$\sigma_{rr}(r,\theta) = \frac{T_x}{2}\left(1 - \frac{R^2}{r^2}\right) + \frac{T_x}{2}\left(1 - 4\frac{R^2}{r^2} + 3\frac{R^4}{r^4}\right)\cos2\theta, \tag{44}$$

$$\sigma_{\theta\theta}(r,\theta) = \frac{T_x}{2}\left(1 + \frac{R^2}{r^2}\right) - \frac{T_x}{2}\left(1 + \frac{3}{4}\frac{R^4}{r^4}\right)\cos2\theta, \tag{45}$$

$$\sigma_{r\theta}(r,\theta) = -\frac{T_x}{2}\left(1 + 2\frac{R^2}{r^2} - 3\frac{R^4}{r^4}\right)\sin2\theta. \tag{46}$$

As shown in Figures 20a and b, we first decompose the geometry into two patches with matched and mismatched parameterizations, respectively. The convergence rates of the stress component σ_{xx} in the L^2-norm are optimal for the global dual mortar method for all cases in Figure 21 and 23 due to the absence of crosspoints. For the matched parameterization case without refinement, the Bézier dual mortar method only achieves optimal rate for $p = 2$, $m : s = 2 : 3$. With one refinement of the dual basis, the proposed method recovers optimal rates for all cases as shown in Figure 22. For mismatched parameterizations without refinement, the Bézier dual mortar method exhibits similar reduced convergence rates as for the matched parameterization case as shown in Figure 23. However, as shown in Figure 24a, after one refinement the proposed method recovers the optimal rates for all degrees, $m : s = 2 : 3$, and refining the dual basis twice results in optimal rates for $p = 2, 3$, $m : s = 3 : 2$, as shown in Figure 24b.

To assess the ability of the method to handle multiple patch coupling the geometry is decomposed into three nonconforming NURBS patches with matched and mismatched parameterizations as shown in Figures 25a and b, respectively. As shown in Figures 26a and 27a, the global dual mortar method suffers from severely deteriorated convergence rates for $p = 2, 3$ and 4 for both matched and mismatched parameterizations due to two types of crosspoints, i.e., the interface/Dirichlet intersections and the interface/interface intersection in the middle. For matched parameterizations

(a) Matched parameterizations
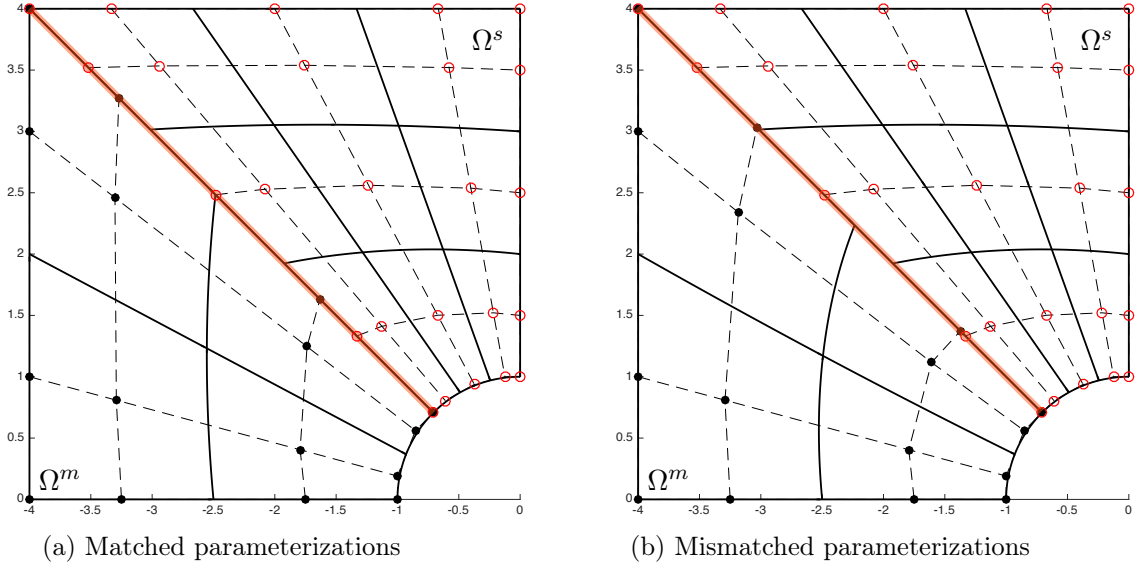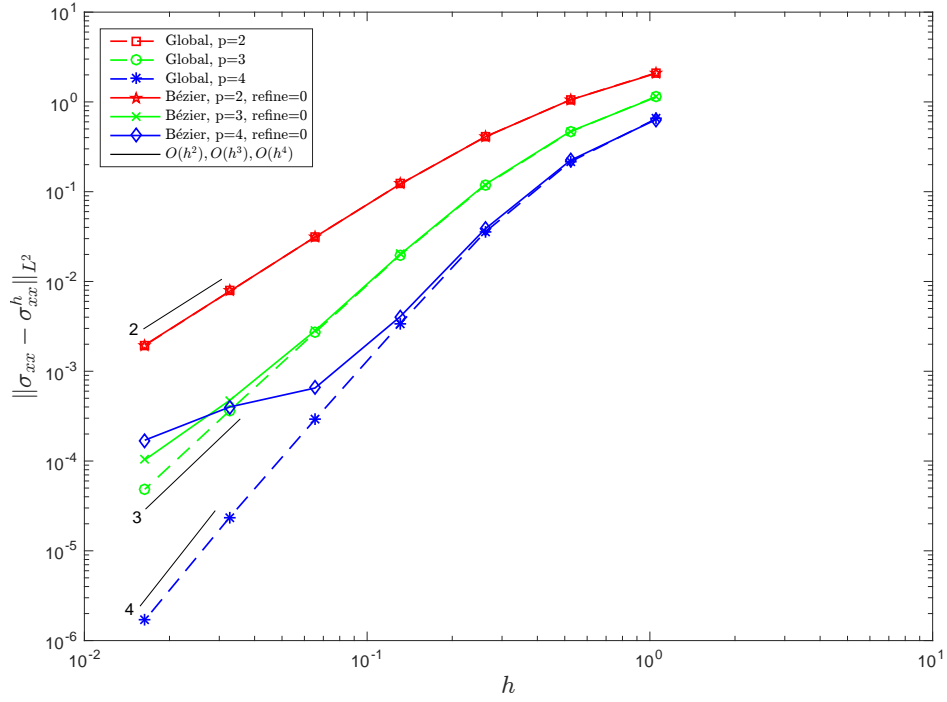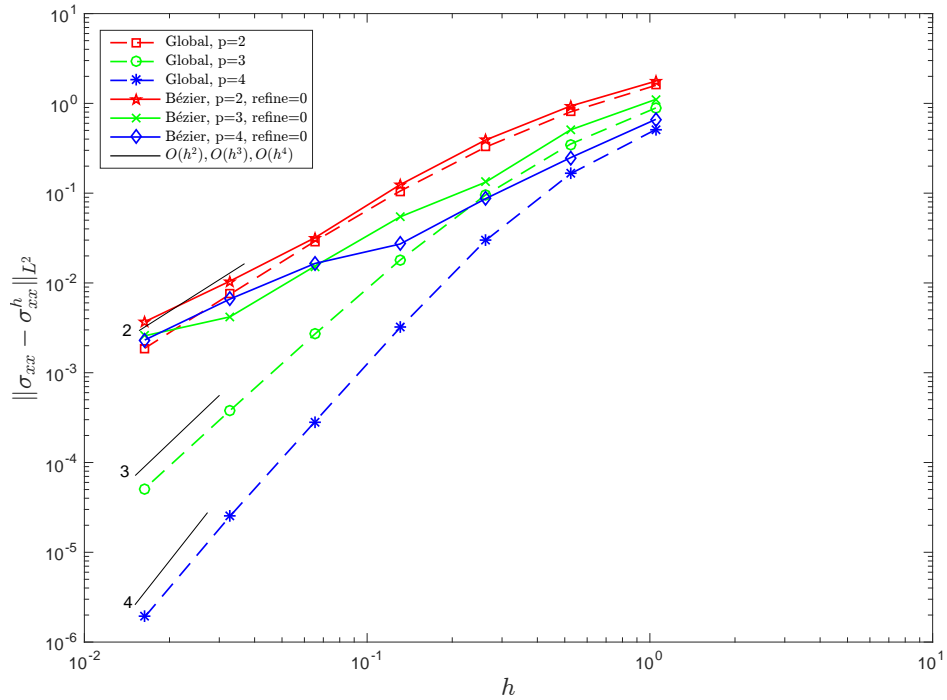
(b) Mismatched parameterizations

Figure 20: NURBS meshes for a quarter plate with a hole.

without refinement, the Bézier dual mortar method achieves optimal rate for $p = 2$, and slightly deteriorated rate for $p = 3$ as shown in Figure 26a. Refining once recovers the optimal rates for $p = 3, 4$ (see Figure 26b). For mismatched parameterizations, optimal rates are achieved for $p = 2$ by refining the dual space once and for $p = 3$ by refining the dual space twice (see Figure 27b). Figure 28 shows plots of the stress component σ_{xx} for both matched and mismatched parameterizations for $p = 2$. It can be seen that even for the coarse initial meshes shown in Figures 25a and b, for both matched and mismatched parameterizations, the stress concentration in the circular cutout is very close to the analytical solution $\sigma_{xx} = 30$, as shown in Figure 28a and Figure 28c.

(a) Master/slave mesh ratio, $m : s = 2 : 3$

(b) Master/slave mesh ratio, $m : s = 3 : 2$

Figure 21: Stress convergence rates for a quarter plate with a circular hole decomposed into two nonconforming NURBS patches with matched parameterizations (see Figure 20a).
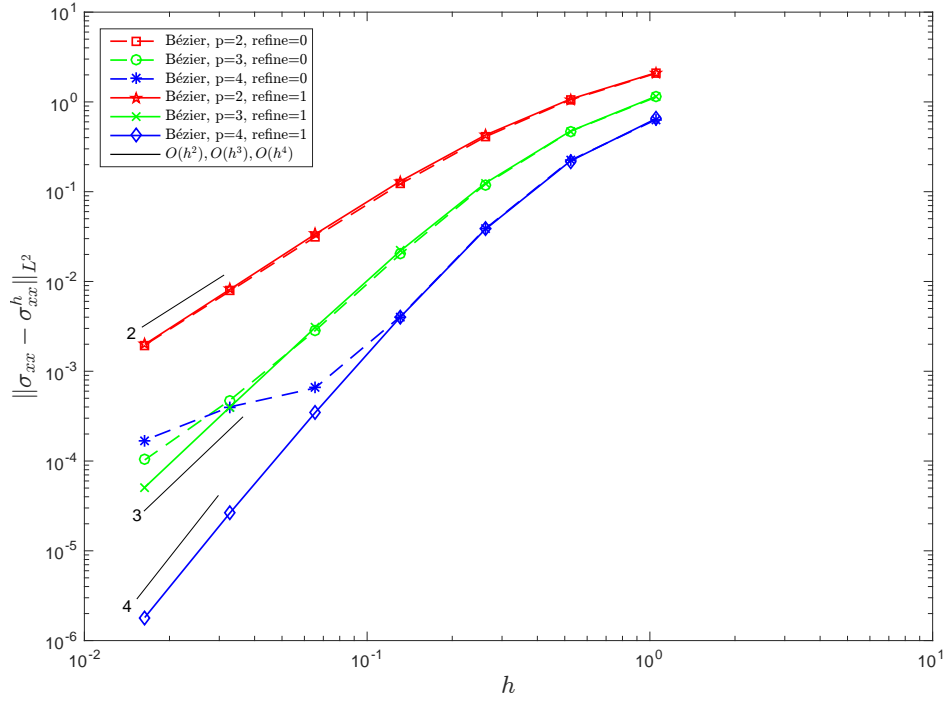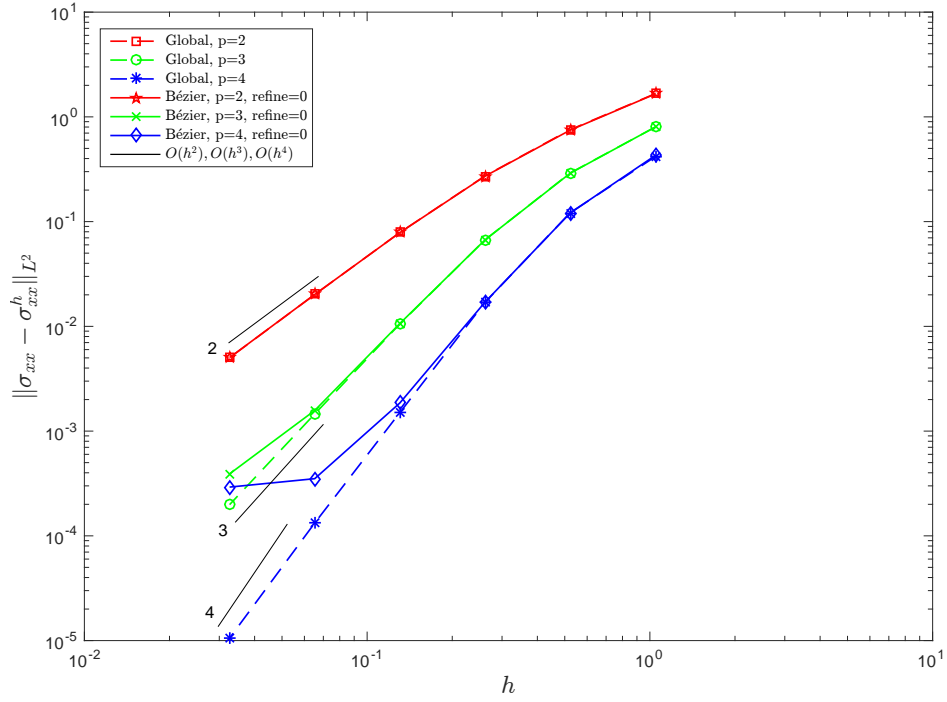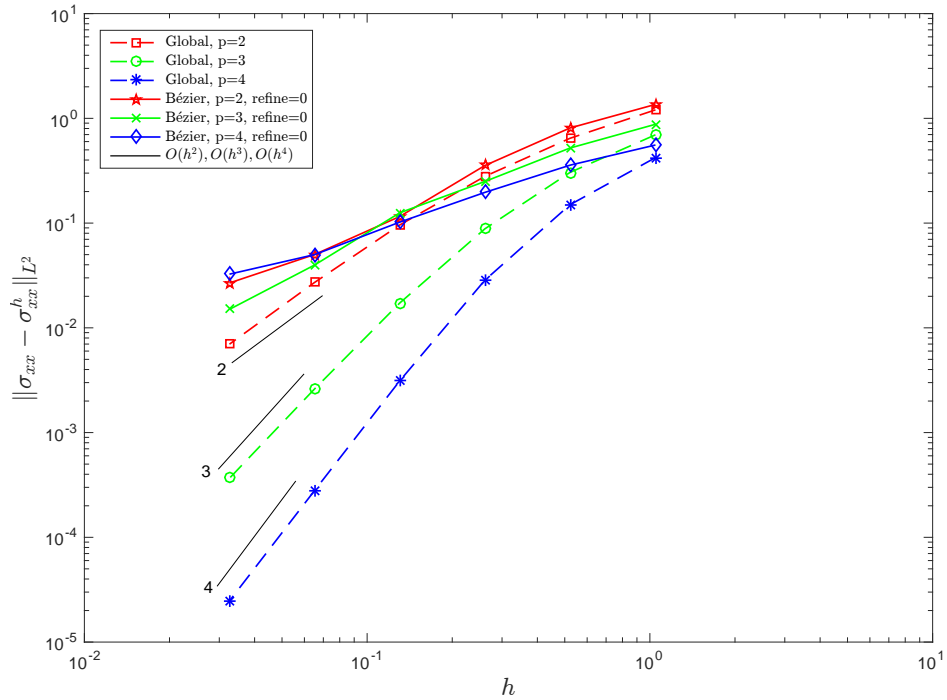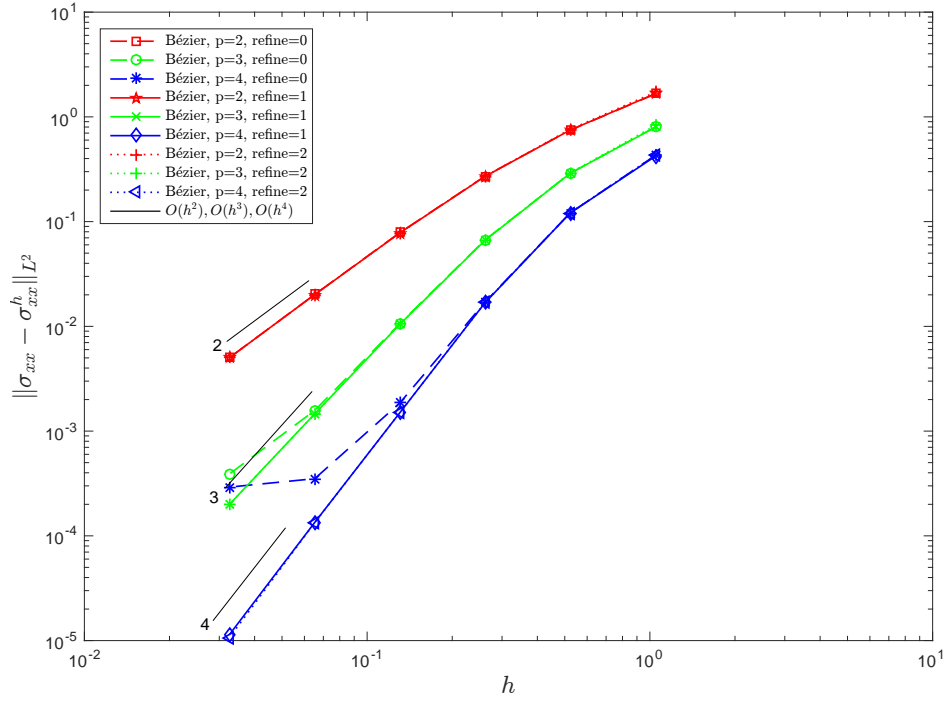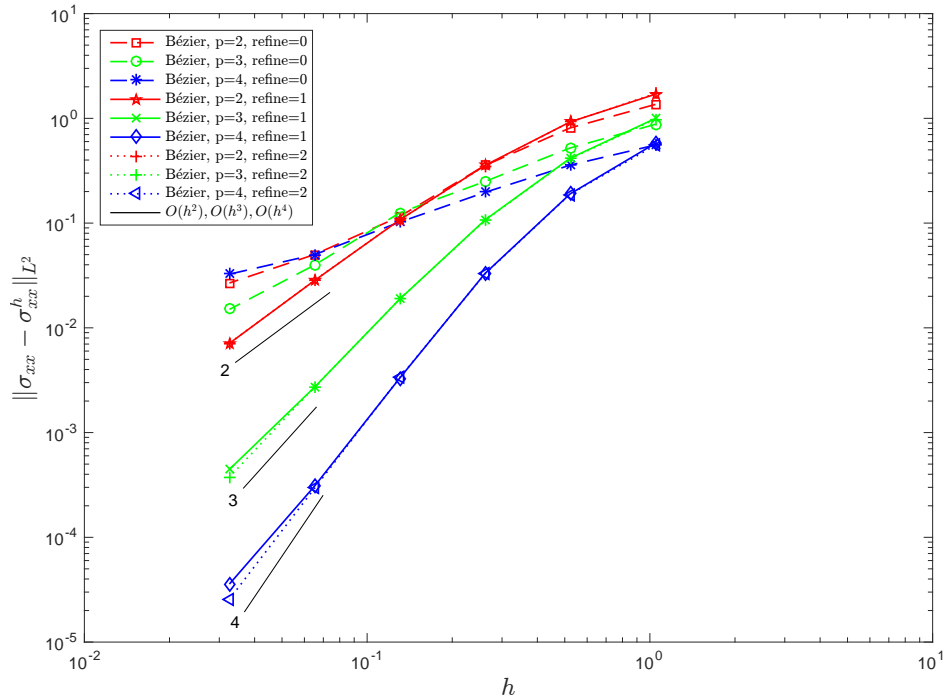
(a) Master/slave mesh ratio, $m : s = 2 : 3$
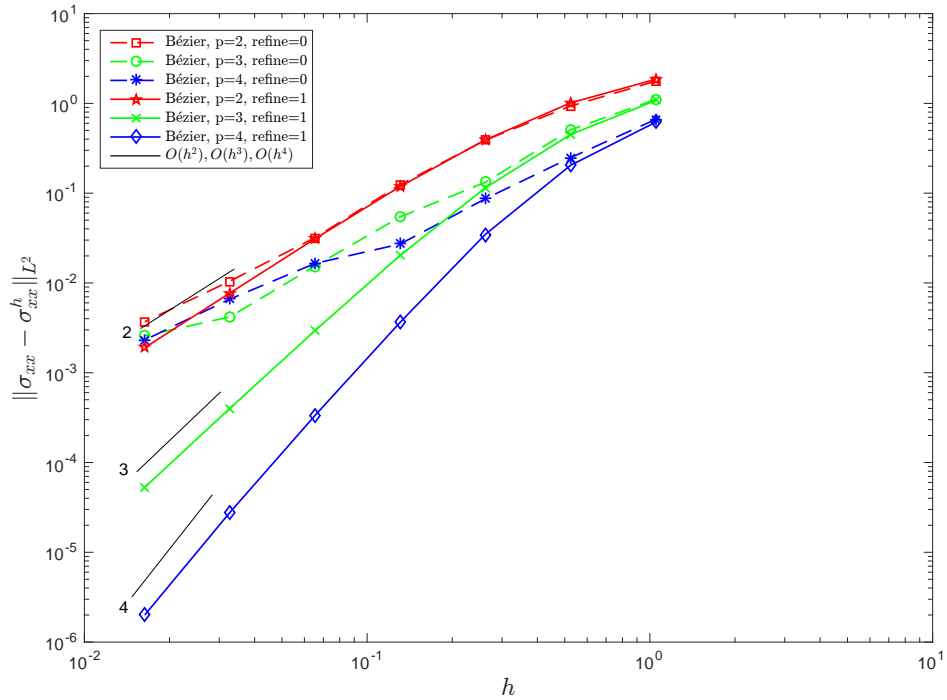
(b) Master/slave mesh ratio, $m : s = 3 : 2$

Figure 22: Stress convergence rates for a quarter plate with a circular hole decomposed into two nonconforming NURBS patches with refined matched parameterizations (see Figure 20a).

(a) Master/slave mesh ratio, $m : s = 2 : 3$

(b) Master/slave mesh ratio, $m : s = 3 : 2$

Figure 23: Stress convergence rates for a quarter plate with a circular hole decomposed into two nonconforming NURBS patches with mismatched parameterizations (see Figure 20b).

(a) Master/slave mesh ratio, $m : s = 2 : 3$

(b) Master/slave mesh ratio, $m : s = 3 : 2$

Figure 24: Stress convergence rates for a quarter plate with a circular hole decomposed into two nonconforming NURBS patches with refined mismatched parameterizations (see Figure 20b).
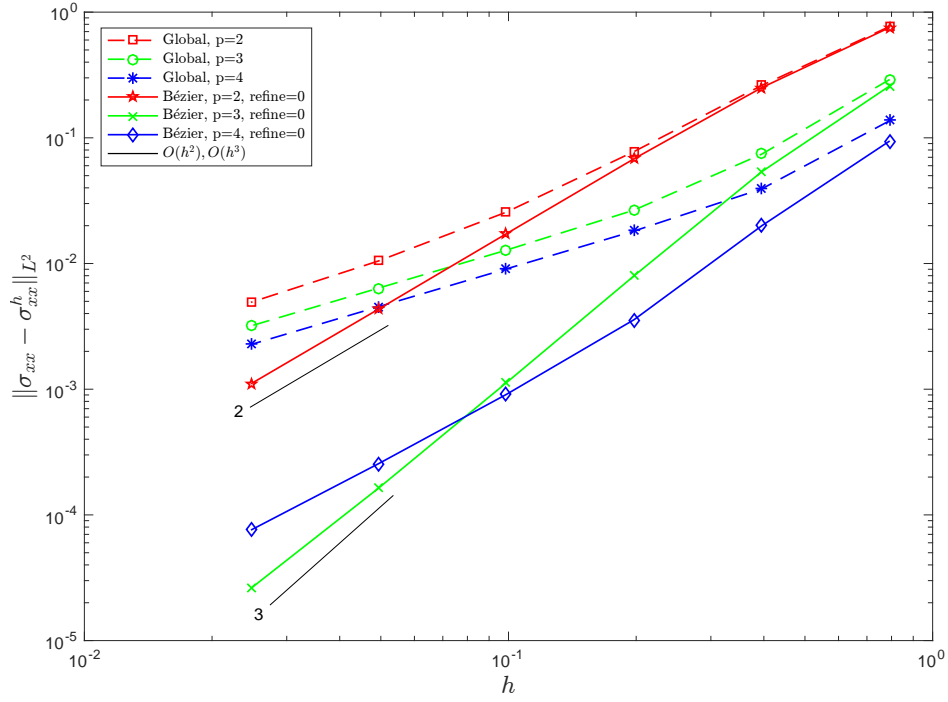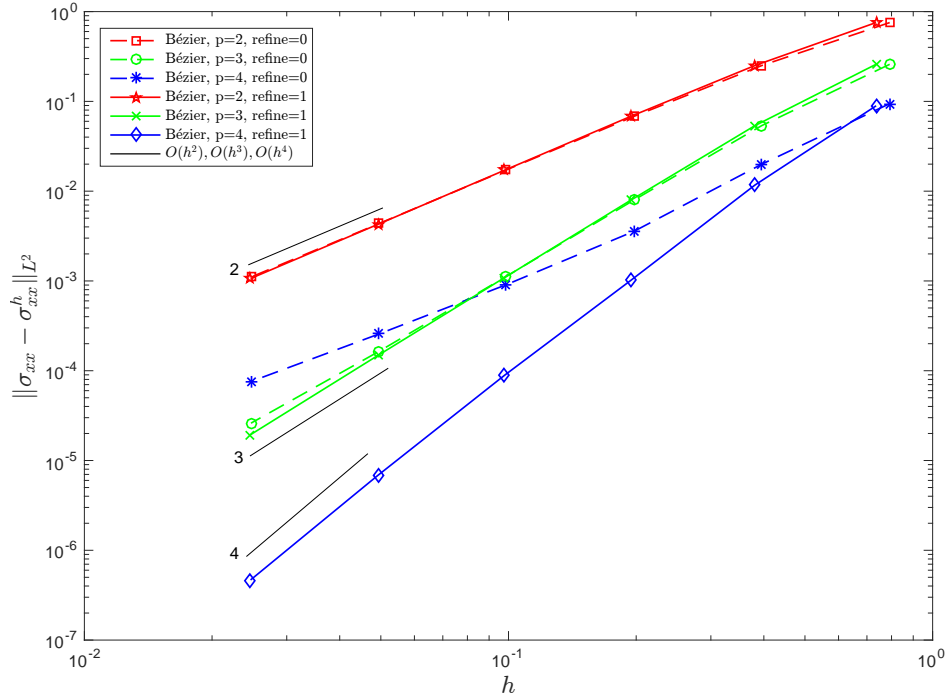
(a) Matched parameterizations   (b) Mismatched parameterizations
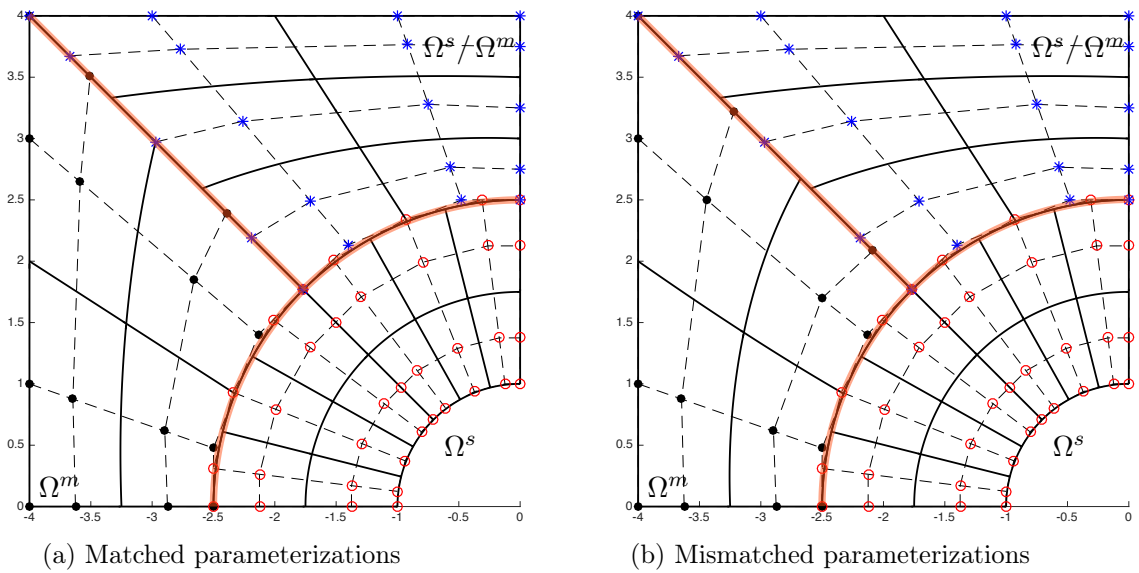
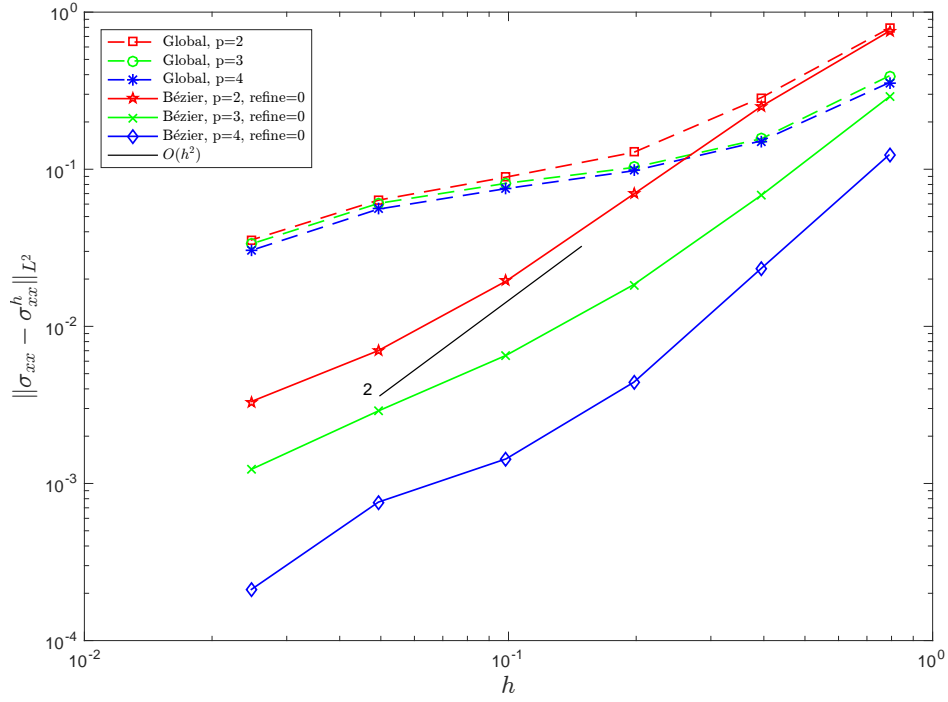Figure 25: NURBS meshes for a quarter plate with a hole.
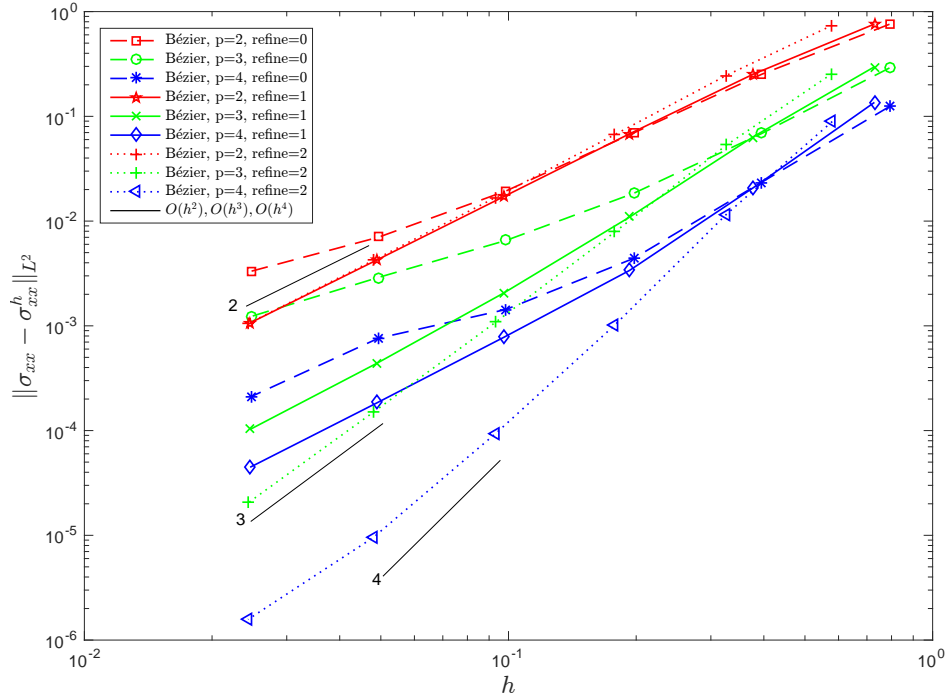
(a) Without refinement

(b) With refinement

Figure 26: Stress convergence rates for a quarter plate with a circular hole decomposed into three nonconforming NURBS patches with matched parameterizations (see Figure 25a).
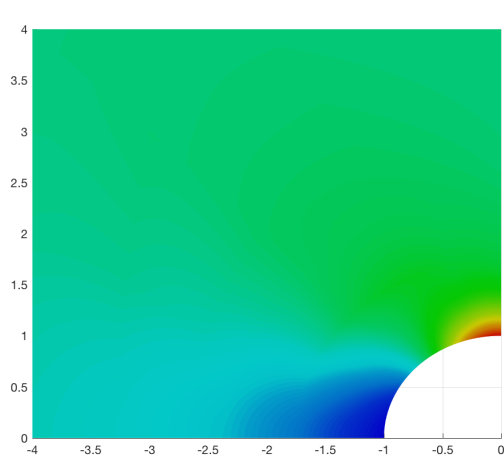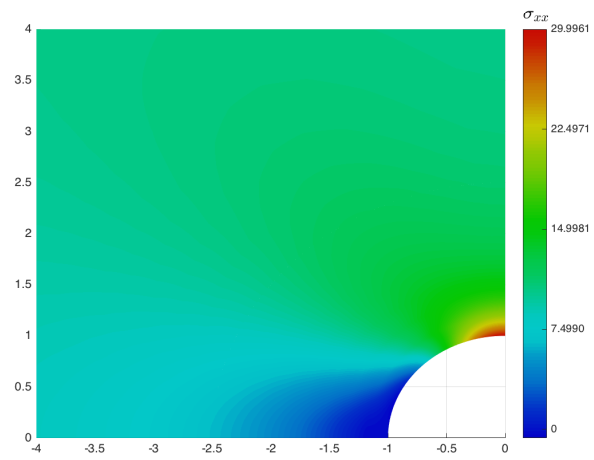
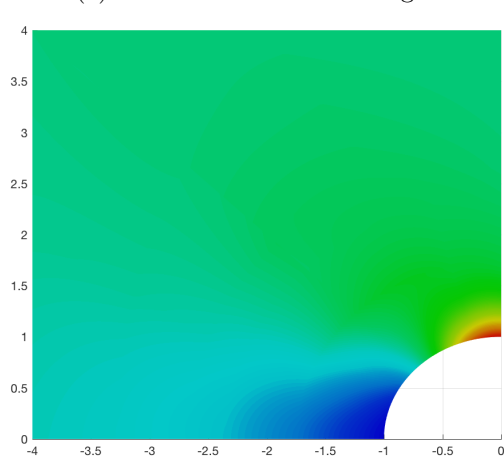(a) Without refinement

(b) With refinements

Figure 27: Stress convergence rates for a quarter plate with a circular hole decomposed into three nonconforming NURBS patches with mismatched parameterizations (see Figure 25b).
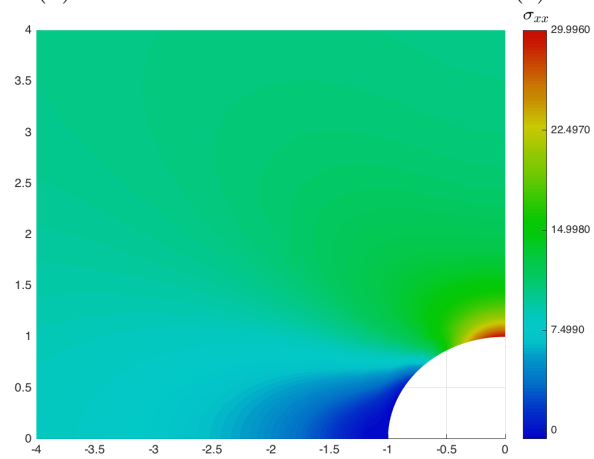
(a) Initial mesh shown in Figure 25a

(b) Mesh after 2 uniform refinements on (a)

(c) Initial mesh shown in Figure 25b

(d) Mesh after 2 uniform refinements on (c)

Figure 28: Stress σ_{xx}, $p = 2$, no refinement of the dual basis space.

6.4 Weakly continuous geometry: Large deformations in two-dimensions

We now employ Bézier dual mortaring to build weakly continuous geometry as described in Section 5. Since the weak continuity constraint is embedded into the geometric description, a standard finite element code can be employed to process the weakly continuous basis in exactly the same manner as a standard conforming basis. To demonstrate the effectiveness of the approach, we compare the displacements computed on a weakly continuous mesh to those computed on a similar continuous mesh for a large deformation, plane strain problem.

The initial geometry and the location of the interface are shown in Figure 29. For the weakly continuous mesh, the discretization does not match at the interface between the two patches and continuity is enforced weakly by building appropriately modified extraction operators. For the continuous mesh, the interface is treated as a C^0 interface. In both cases, the basis functions are quadratic maximally smooth B-splines. A Bézier element representation of the coarsest weakly continuous mesh is also shown in Figure 29. As can be seen, there is one additional element on the right side of the interface in the vertical direction. As the mesh is refined, the size of the elements on the left side of the interface is cut in half in each direction and the right side is refined so that there is always one additional element in the vertical direction. The continuous meshes are refined such that the element size is always the same as the element size on the left side of the weakly continuous meshes for a given refinement level.
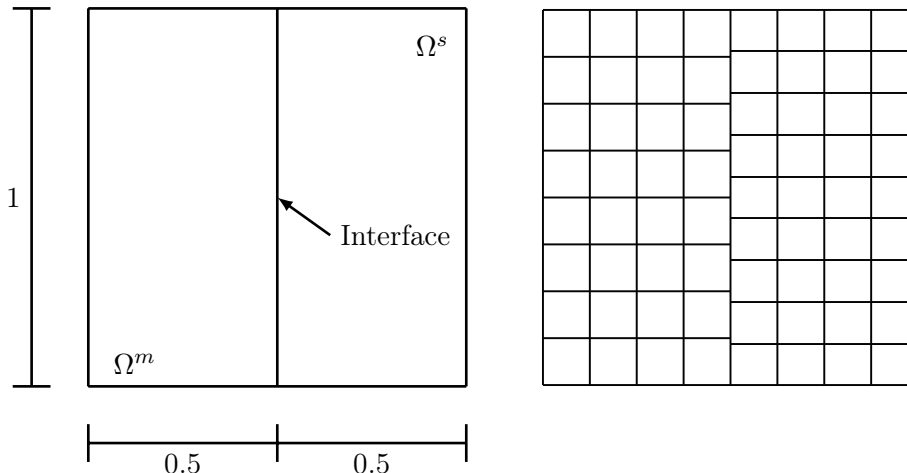

Figure 29: The geometry and Bézier mesh.

We compare the computed results for the three load cases with associated boundary conditions that are shown in Figure 30. The deformation is governed by the strain energy density functional that is given by

$$\psi = \lambda \left(\tfrac{1}{4}(J^2 - 1) - \tfrac{1}{2}\ln J \right) + \tfrac{1}{2}\mu \left(\text{tr}\,[\mathbf{b}] - 3 - 2\ln J \right) \tag{47}$$

where λ and μ are the typical Lamé parameters with

$$\lambda = \frac{E\nu}{(1 + \nu)(1 - 2\nu)} \tag{48}$$

$$\mu = \frac{E}{2(1 + \nu)} \tag{49}$$

for Young's Modulus, E, and Poison's ratio, ν. We use $E = 30 \times 10^9$ and $\nu = 0.48$ for the results presented here. In addition,

$$J = |\mathbf{F}| \quad \text{and} \quad \mathbf{b} = \mathbf{F}\mathbf{F}^{\mathrm{T}} \tag{50}$$

where $\mathbf{F}$ is the deformation gradient, and $\mathbf{b}$ is the left Cauchy-Green tensor.

The pressure boundary condition, p, is applied as a dead load in the reference configuration and is increased in twenty equal load increments to a maximum value of 100×10^9. At each load increment, the nonlinear problem is solved using a Newton-Raphson scheme with convergence satisfied when the residual is reduced by a factor of 10^8.
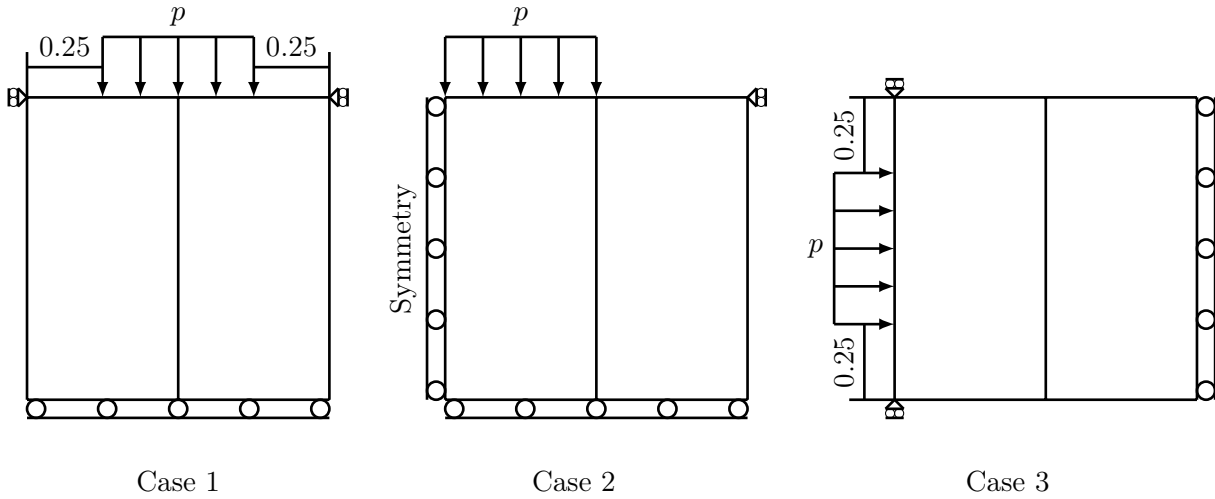

Figure 30: Load cases

The results of the computations are shown in Figures 31 through 33. Each figure shows the unscaled deformation at the final load increment. On the left, the color scale indicates the magnitude of the displacement. On the right, each patch is shown as a distinct color so that the deformation of the interface between the two patches can clearly be seen. In all cases, the deformation of the interface is severe, but there is nothing in the displacement plot that indicates the presence of the weak interface.

To quantify the accuracy of the weak geometry approach we compare the displacements, $u^{h,w}$, computed on the weakly continuous mesh to the displacements, $u^{h,c}$, computed on the continuous mesh. We define the relative error, e_r, to be the L^2-norm of the difference between the two considered
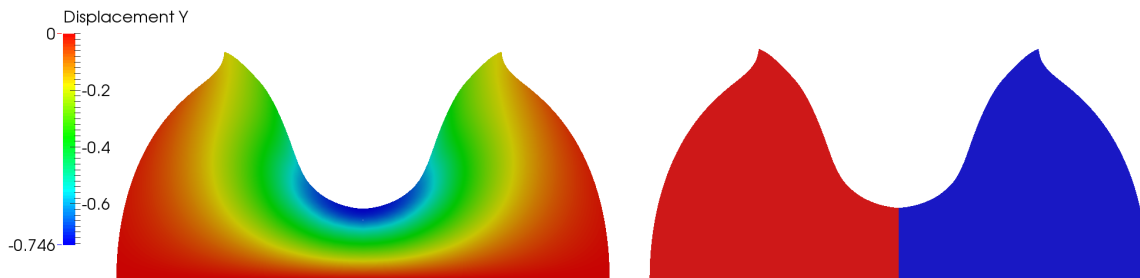

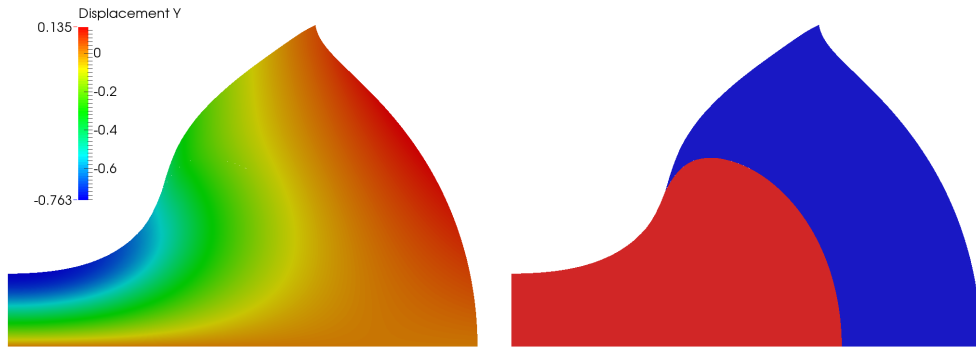Figure 31: Vertical displacement and deformed configuration - Case 1.

40

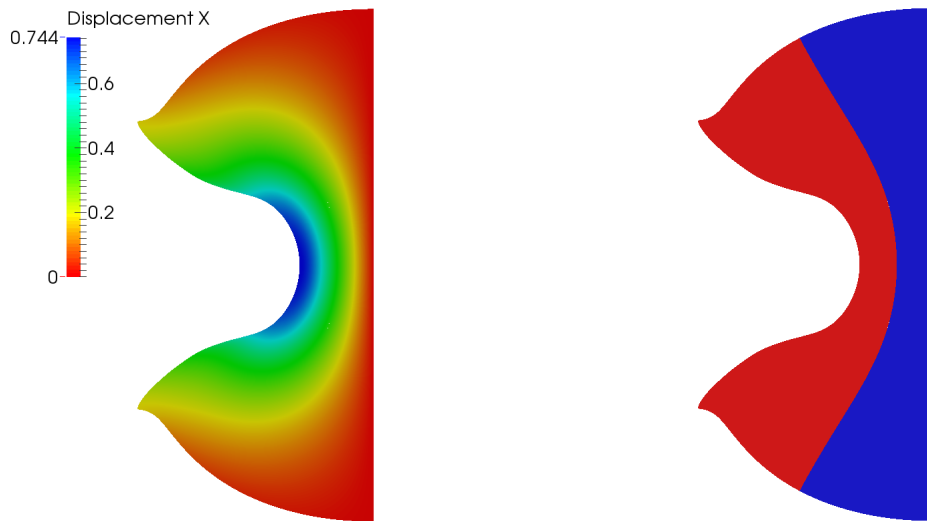Figure 32: Vertical displacement and deformed configuration - Case 2.

Figure 33: Horizontal displacement and deformed configuration - Case 3.

displacements, i.e

$$e_r = \|u^{h,w} - u^{h,c}\|_{L^2}. \tag{51}$$

Using the triangle inequality,

$$\|u^{h,w} - u\|_{L^2} \leq \|u^{h,w} - u^{h,c}\|_{L^2} + \|u^{h,c} - u\|_{L^2}, \tag{52}$$

we see that the absolute error of the solution computed on the weakly continuous mesh case is bounded by the sum of the relative error and the absolute error of the solution computed on the continuous mesh case. Now, assuming that the solution computed on the continuous mesh case converges optimally, by (52), if the relative error converges optimally then we know that the absolute error of the solution computed on the weakly continuous mesh case also must converge optimally. The convergence rates of the relative error of the last load step are plotted in Figure 34 for the three load cases. This figure clearly shows that the convergence rate of the relative error are cubic, which is the optimal rate for quadratic basis functions.
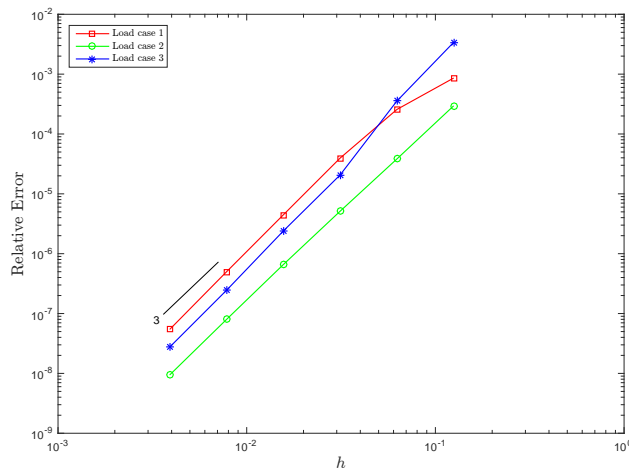

Figure 34: Convergence rates of the L^2-relative error of the last load step for the three large deformation load cases.

7 Conclusions

We have introduced a new approach for the coupling of non-conforming higher-order smooth spline patches which we call the isogeometric Bézier dual mortar method. The construction of the underlying dual spline basis is based on Bézier extraction and projection and is applicable to any spline description which has a Bézier representation. The dual basis is refineable and the associated mortaring strategy preserves the sparsity of the stiffness matrix. The accuracy of the coupling can be adaptively controlled by employing a dual basis refinement scheme which can be used to recover optimal convergence rates without adding any additional degrees-of-freedom to the global system. As a particular application of Bézier dual mortaring, we introduced weakly continuous geometry, where the weak continuity constraint is built into properly modified extraction operators. This allows for the use of weakly coupled multi-patch geometry in design and as a basis for standard finite element frameworks which do not employ any mortaring algorithms.

We applied the isogeometric Bézier dual mortar method to standard linear and nonlinear elastic test cases and B-spline and NURBS geometries. All tests show that the isogeometric Bézier dual

mortar method is robust and accurate, works for arbitrary master/slave pairings, and arbitrary parameterizations.

Acknowledgments

References

[1] T. J. R. Hughes, J. A. Cottrell, Y. Bazilevs, Isogeometric analysis: CAD, finite elements, NURBS, exact geometry and mesh refinement, Computer methods in applied mechanics and engineering 194 (39) (2005) 4135–4195.

[2] J. A. Cottrell, T. J. R. Hughes, Y. Bazilevs, Isogeometric analysis: Toward Integration of CAD and FEA, Wiley, Chichester, 2009.

[3] J. A. Cottrell, T. J. R. Hughes, A. Reali, Studies of refinement and continuity in isogeometric structural analysis, Computer Methods in Applied Mechanics and Engineering 196 (41) (2007) 4160 – 4183.

[4] T. J. R. Hughes, J. A. Evans, A. Reali, Finite element and NURBS approximations of eigenvalue, boundary-value, and initial-value problems, Computer Methods in Applied Mechanics and Engineering 272 (2014) 290 – 320.

[5] A. Apostolatos, R. Schmidt, R. Wüchner, K.-U. Bletzinger, A Nitsche-type formulation and comparison of the most common domain decomposition methods in isogeometric analysis, International Journal for Numerical Methods in Engineering 97 (7) (2014) 473–504.

[6] M. Breitenberger, A. Apostolatos, B. Philipp, R. Wüchner, K.-U. Bletzinger, Analysis in computer aided design: Nonlinear isogeometric B-Rep analysis of shell structures, Computer Methods in Applied Mechanics and Engineering 284 (2015) 401 – 457.

[7] Y. Guo, M. Ruess, Nitsche's method for a coupling of isogeometric thin shells and blended shell structures, Computer Methods in Applied Mechanics and Engineering 284 (2015) 881–905.

[8] M. Ruess, D. Schillinger, A. I. Özcan, E. Rank, Weak coupling for isogeometric analysis of non-matching and trimmed multi-patch geometries, Computer Methods in Applied Mechanics and Engineering 269 (2014) 46–71.

[9] C. Hesch, P. Betsch, Isogeometric analysis and domain decomposition methods, Computer Methods in Applied Mechanics and Engineering 213-216 (2012) 104–112.

[10] W. Dornisch, G. Vitucci, S. Klinkel, The weak substitution method–an application of the mortar method for patch coupling in NURBS-based isogeometric analysis, International Journal for Numerical Methods in Engineering 103 (3) (2015) 205–234.

[11] L. Coox, F. Greco, O. Atak, D. Vandepitte, W. Desmet, A robust patch coupling method for NURBS-based isogeometric analysis of non-conforming multipatch surfaces, Computer Methods in Applied Mechanics and Engineering 316 (2017) 235 – 260.

[12] V. P. Nguyen, P. Kerfriden, M. Brino, S. P. A. Bordas, E. Bonisoli, Nitsche's method for two and three dimensional NURBS patch coupling, Computational Mechanics 53 (6) (2014) 1163–1182.

[13] A. Seitz, P. Farah, J. Kremheller, B. I. Wohlmuth, W. A. Wall, A. Popp, Isogeometric dual mortar methods for computational contact mechanics, Computer Methods in Applied Mechanics and Engineering 301 (2016) 259 – 280.

[14] W. Dornisch, J. Stöckler, R. Müller, Dual and approximate dual basis functions for B-splines and NURBS – Comparison and application for an efficient coupling of patches with the isogeometric mortar method, Computer Methods in Applied Mechanics and Engineering 316 (2017) 449 – 496.

[15] E. Brivadis, A. Buffa, B. I. Wohlmuth, L. Wunderlich, Isogeometric mortar methods, Computer Methods in Applied Mechanics and Engineering 284 (2015) 292 – 319.

[16] D. C. Thomas, M. A. Scott, J. A. Evans, K. Tew, E. Evans, Bézier projection: A unified approach for local projection and quadrature-free refinement and coarsening of NURBS and T-splines with particular application to isogeometric design and analysis, Computer Methods in Applied Mechanics and Engineering 284 (2015) 55–105.

[17] I. Babuška, The finite element method with penalty, Mathematics of computation 27 (122) (1973) 221–228.

[18] F. B. Belgacem, The Mortar finite element method with Lagrange multipliers, Numerische Mathematik 84 (2) (1999) 173–197.

[19] D. Boffi, F. Brezzi, M. Fortin, Mixed Finite Element Methods and Applications, Springer, Berlin, 2013.

[20] W. Dornisch, S. Klinkel, Boundary Conditions and Multi-Patch Connections in Isogeometric Analysis, PAMM 11 (1) (2011) 207–208.

[21] J. Nitsche, Über ein Variationsprinzip zur Lösung von Dirichlet-Problemen bei Verwendung von Teilräumen, die keinen Randbedingungen unterworfen sind, Abhandlungen aus dem Mathematischen Seminar der Universität Hamburg 36 (1) (1971) 9–15.

[22] C. Bernardi, Y. Maday, A. T. Patera, Domain decomposition by the mortar element method, in: Asymptotic and numerical methods for partial differential equations with critical parameters, Springer, 269–286, 1993.

[23] C. Bernardi, Y. Maday, A. T. Patera, A new nonconforming approach to domain decomposition: the mortar element method, Nonliner Partial Differential Equations and Their Applications (1994) 13–51.

[24] B. I. Wohlmuth, A mortar finite element method using dual spaces for the Lagrange multiplier, SIAM journal on numerical analysis 38 (3) (2000) 989–1012.

[25] B. I. Wohlmuth, Discretization Methods and Iterative Solvers Based on Domain Decomposition, vol. 17, Springer, Berlin, 2001.

[26] B. P. Lamichhane, B. I. Wohlmuth, Higher order dual Lagrange multiplier spaces for mortar finite element discretizations, CALCOLO 39 (4) (2002) 219–237.

[27] P. Oswald, B. I. Wohlmuth, On polynomial reproduction of dual FE bases, in: Thirteenth international conference on domain decomposition methods, 85–96, 2001.

[28] C. de Boor, G. Fix, Spline approximation by quasiinterpolants, Journal of Approximation Theory 8 (1) (1973) 19 – 45.

[29] C. De Boor, On local linear functionals which vanish at all B-splines but one, Mathematics Research Center, University of Wisconsin, 1975.

[30] L. Schumaker, Spline functions: basic theory, Cambridge University Press, 2007.

[31] C. K. Chui, W. He, J. Stöckler, Nonstationary tight wavelet frames, I: Bounded intervals, Applied and Computational Harmonic Analysis 17 (2) (2004) 141 – 197.

[32] R. T. Farouki, C. A. Neff, On the numerical condition of Bernstein-Bézier subdivision processes, Mathematics of Computation 55 (192) (1990) 637–647.

[33] M. J. Borden, M. A. Scott, J. A. Evans, T. J. R. Hughes, Isogeometric finite element data structures based on Bézier extraction of NURBS, International Journal for Numerical Methods in Engineering 87 (1-5) (2011) 15–47.

[34] M. A. Scott, M. J. Borden, C. V. Verhoosel, T. W. Sederberg, T. J. R. Hughes, Isogeometric finite element data structures based on Bézier extraction of T-splines, International Journal for Numerical Methods in Engineering 88 (2) (2011) 126–156.

[35] L. Piegl, W. Tiller, The NURBS Book, Springer-Verlag, New York, 1997.

[36] B. I. Wohlmuth, A. Popp, M. W. Gee, W. A. Wall, An abstract framework for a priori estimates for contact problems in 3D with quadratic finite elements, Computational Mechanics 49 (6) (2012) 735–747.

[37] M. A. Scott, X. Li, T. W. Sederberg, T. J. R. Hughes, Local Refinement of Analysis-Suitable T-splines, Computer Methods in Applied Mechanics and Engineering 213 (2012) 206 – 222.

A A derivation of the weakly continuous extraction operator for element e_{21} from Figure 3.

For the example shown in Figure 3, the basis relation matrix $\mathbf{G}_{\bar{N}^r,N^m}$ defined by (37) and the localized counterpart $\mathbf{G}^e_{\bar{N}^r,N^m}$ for the interface of element e_{21} are

$$\mathbf{G}_{\bar{N}^r,N^m} = \begin{bmatrix} 1 & \frac{1}{3} & 0 & 0 & 0 & 0 \\ 0 & \frac{2}{3} & \frac{2}{3} & \frac{1}{3} & 0 & 0 \\ 0 & 0 & \frac{1}{3} & \frac{2}{3} & \frac{2}{3} & 0 \\ 0 & 0 & 0 & 0 & \frac{1}{3} & 1 \end{bmatrix}^{\mathrm{T}} \quad \text{and} \quad \mathbf{G}^e_{\bar{N}^r,N^m} = \begin{bmatrix} \frac{1}{3} & \frac{2}{3} & 0 \\ 0 & \frac{2}{3} & \frac{1}{3} \\ 0 & \frac{1}{3} & \frac{2}{3} \end{bmatrix}. \tag{53}$$

The standard Bézier extraction operator $\mathbf{R}^{e,r}_{\xi_1}$ and the basis transformation matrix $\mathbf{M}$ are

$$\mathbf{R}^{e,r}_{\xi_1} = \begin{bmatrix} \frac{1}{3} & 0 & 0 \\ \frac{2}{3} & 1 & \frac{1}{2} \\ 0 & 0 & \frac{1}{2} \end{bmatrix} \quad \text{and} \quad \mathbf{M} = \begin{bmatrix} 1 & 0 & 0 \\ \frac{1}{2} & \frac{1}{2} & 0 \\ \frac{1}{4} & \frac{1}{2} & \frac{1}{4} \end{bmatrix}, \tag{54}$$

and the weakly continuous one-dimensional interface element extraction operator $\tilde{\mathbf{R}}^e_{\xi_1}$ for element e_{21} is

$$\tilde{\mathbf{R}}^e_{\xi_1} = (\mathbf{G}^e_{\bar{N}^r,N^m})^{\mathrm{T}} \mathbf{R}^{e,r}_{\xi_1} \mathbf{M}^{-\mathrm{T}} = \begin{bmatrix} \frac{1}{9} & -\frac{1}{9} & \frac{1}{9} \\ \frac{2}{3} & \frac{2}{3} & 0 \\ \frac{2}{9} & \frac{4}{9} & \frac{8}{9} \end{bmatrix}. \tag{55}$$

The two standard one-dimensional Bézier extraction operators for the original slave patch element e_2 are

$$\mathbf{R}^e_{\xi_1} = \begin{bmatrix} \frac{1}{2} & 0 & 0 \\ \frac{1}{2} & 1 & \frac{1}{2} \\ 0 & 0 & \frac{1}{2} \end{bmatrix} \quad \text{and} \quad \mathbf{R}^e_{\xi_2} = \begin{bmatrix} \frac{1}{2} & 0 & 0 \\ \frac{1}{2} & 1 & 0 \\ 0 & 0 & 1 \end{bmatrix}. \tag{56}$$

As shown in Figure 3, the interior basis functions of element e_{21} are identical to those of element e_2, and only the interface basis functions are replaced by the refined interface basis. We decompose $\mathbf{R}^e_{\xi_2}$ into two submatrices $\mathbf{R}_1$ and $\mathbf{R}_2$ such that

$$\mathbf{R}^e_{\xi_2} = \begin{bmatrix} \mathbf{R}_1 \\ \hline \mathbf{R}_2 \end{bmatrix} = \begin{bmatrix} \frac{1}{2} & 0 & 0 \\ \frac{1}{2} & 1 & 0 \\ \hline 0 & 0 & 1 \end{bmatrix}, \tag{57}$$

where $\mathbf{R}_1$ is related to the interior basis functions and $\mathbf{R}_2$ is related to the interface basis functions. Then, the weakly continuous patch element extraction operator $\tilde{\mathbf{R}}^e$ for element e_{21} can be computed

as follows:

$$\tilde{\mathbf{R}}^e = \begin{bmatrix} \mathbf{R}_1 \otimes \mathbf{R}_{\xi_1}^e \\ \mathbf{R}_2 \otimes \tilde{\mathbf{R}}_{\xi_1}^e \end{bmatrix} = \begin{bmatrix} \frac{1}{2}\mathbf{R}_{\xi_1}^e & 0 & 0 \\ \frac{1}{2}\mathbf{R}_{\xi_1}^e & \mathbf{R}_{\xi_1}^e & 0 \\ 0 & 0 & \tilde{\mathbf{R}}_{\xi_1}^e \end{bmatrix} = \begin{bmatrix} \frac{1}{4} & 0 & 0 & 0 & 0 & 0 & 0 & 0 & 0 \\ \frac{1}{4} & \frac{1}{2} & \frac{1}{4} & 0 & 0 & 0 & 0 & 0 & 0 \\ 0 & 0 & \frac{1}{4} & 0 & 0 & 0 & 0 & 0 & 0 \\ \frac{1}{4} & 0 & 0 & \frac{1}{2} & 0 & 0 & 0 & 0 & 0 \\ \frac{1}{4} & \frac{1}{2} & \frac{1}{4} & \frac{1}{2} & 1 & \frac{1}{2} & 0 & 0 & 0 \\ 0 & 0 & \frac{1}{4} & 0 & 0 & \frac{1}{2} & 0 & 0 & 0 \\ 0 & 0 & 0 & 0 & 0 & 0 & \frac{1}{9} & -\frac{1}{9} & \frac{1}{9} \\ 0 & 0 & 0 & 0 & 0 & 0 & \frac{2}{3} & \frac{2}{3} & 0 \\ 0 & 0 & 0 & 0 & 0 & 0 & \frac{2}{9} & \frac{4}{9} & \frac{8}{9} \end{bmatrix}. \tag{58}$$

Note that the only difference between the weakly continuous element extraction operator and the standard element extraction operator is that the last three rows are modified. These rows correspond to interface basis functions.